Inorganic Chemistry

pubs.acs.org/IC Article

Ru(II) Oligothienyl Complexes with Fluorinated Ligands: Photophysical, Electrochemical, and Photobiological Properties

Houston D. Cole, Abbas Vali, John A. Roque, III, Ge Shi, Alisher Talgatov, Gurleen Kaur, Antonio Francés-Monerris, Marta E. Alberto,* Colin G. Cameron,* and Sherri A. McFarland*

Cite This: https://doi.org/10.1021/acs.inorgchem.3c04382 Read Online

ACCESS | Metrics & More | Article Recommendations | Supporting Information

Downloaded via UNIV OF TEXAS AT ARLINGTON on May 10, 2024 at 21:22:28 (UTC).
See https://pubs.acs.org/sharingguidelines for options on how to legitimately share published articles.

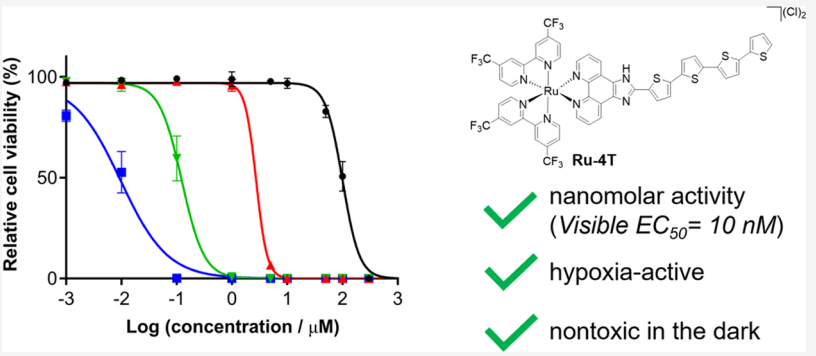

ABSTRACT: A series of Ru(II) complexes incorporating two 4,4′-bis(trifluoromethyl)-2,2′-bipyridine (4,4′-btfmb) coligands and thienyl-appended imidazo[4,5-*f*][1,10]phenanthroline (IP-*n*T) ligands was characterized and assessed for phototherapy effects toward cancer cells. The $[Ru(4,4'\text{-btfmb})_2(\text{IP-}n\text{T})]^{2+}$ scaffold has greater overall redox activity compared to Ru(II) polypyridyl complexes such as $[Ru(bpy)_3]^{2+}$. **Ru-1T−Ru-4T** have additional oxidations due to the *n*T group and additional reductions due to the 4,4′-btfmb ligands. **Ru-2T−Ru-4T** also exhibit *n*T-based reductions. **Ru-4T** exhibits two oxidations and eight reductions within the potential window of −3 to +1.5 V. The lowest-lying triplets (T_1) for **Ru-0T−2T** are metal-to-ligand charge-transfer (^{3}MLCT) excited states with lifetimes around 1 μs, whereas T_1 for **Ru-3T−4T** is longer-lived (∼20−24 μs) and of significant intraligand charge-transfer (^{3}ILCT) character. Phototoxicity toward melanoma cells (SK-MEL-28) increases with *n*, with **Ru-4T** having a visible EC_{50} value as low as 9 nM and PI as large as 12,000. **Ru-3T** and **Ru-4T** retain some of this activity in hypoxia, where **Ru-4T** has a visible EC_{50} as low as 35 nM and PI as high as 2900. Activity over six biological replicates is consistent and within an order of magnitude. These results demonstrate the importance of lowest-lying ^{3}ILCT states for phototoxicity and maintaining activity in hypoxia.

1. INTRODUCTION

Cancer continues to be a leading cause of mortality worldwide.[1] Despite substantial progress in available medical treatments,[2−6] there remains a critical need for innovative therapeutic strategies and adjuvants to complement traditional methods like surgery, radiotherapy, and chemotherapy. In this regard, photodynamic therapy (PDT) is a possible avenue for targeted cancer therapy. It employs a nontoxic photosensitizer (PS), light, and molecular oxygen to produce cytotoxic reactive oxygen species (ROS), importantly singlet oxygen ($^1O_2$), that destroy tumors and tumor vasculature and can induce antitumor immunity.[7−10] Phototoxic effects are restricted to oxygenated areas where light is delivered and PS has accumulated. The localized action of PDT results in fewer side effects and improved quality of life for patients.[11,12] PDT can be enhanced by tumor-selective PSs and precise delivery of light. In addition, the light protocol can be optimized by altering the drug-to-light interval (DLI) and tuning the wavelength, fluence, and irradiance.

There is also a drive to develop light-responsive compounds that generate ROS at low oxygen tension or function via alternate mechanisms that complement the $^1O_2$ pathway. This capacity would allow effective treatment of hypoxic tumors and the use of high light irradiance. Metal complexes, particularly Ru(II) polypyridyl systems, are of significant interest in this regard. The strategic combination of ligands and metals allows access to a range of excited-state configurations with unique photophysical characteristics. Approaches have included the

Received: December 9, 2023
Revised: April 14, 2024
Accepted: April 17, 2024

© XXXX American Chemical Society

Chart 1. (a) Structure of Racemic TLD1433 and (b) Structures of Racemic Complexes in This Study

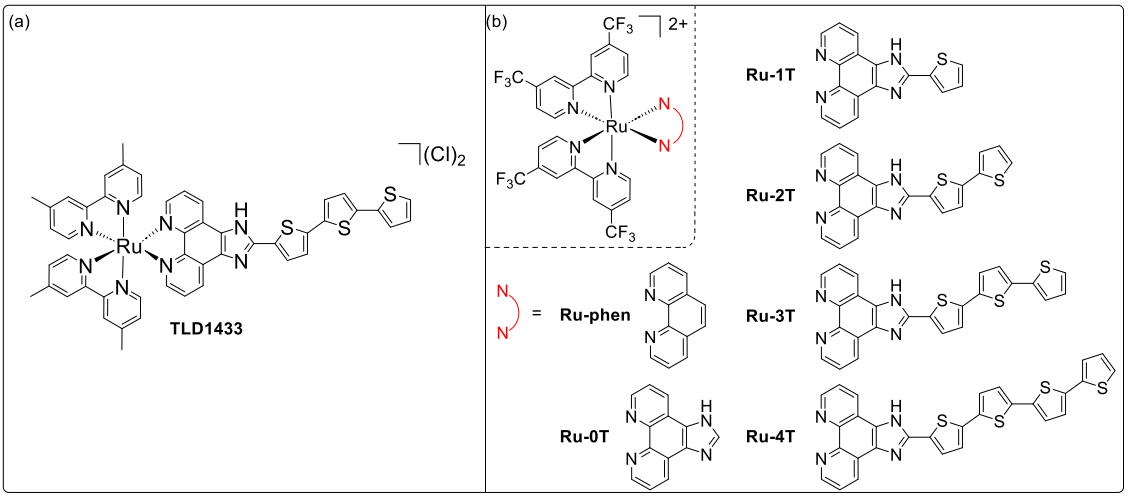

photorelease of bulky ligands to expose phototoxic metals and/or ligands,[13−21] photocaging of chemotherapeutics and enzyme inhibitors,[18,22−43] photoredox reactions,[44,45] and enhancing ROS production even under low oxygen conditions.[17,20,46]

Our research group has a strong focus on metal complexes as PSs for their diverse mechanisms of action. Their modular design and relatively straightforward synthesis allow for rapid alteration of their physicochemical, photophysical, and biological characteristics and aligns with our tumor-specific approach to PS development. We advocate that no singular ideal PS exists; rather, PS design should be tailored to the intended application. Our Ru(II) polypyridyl complex, TLD1433, is a prime example, currently in Phase II clinical trials for treating nonmuscle invasive bladder cancer (NMIBC) with PDT (Chart 1a).[11,47,48] It exhibits significant phototoxicity toward cancer cells while maintaining low dark toxicity. Clinically, it is activated using green light to prevent harm to underlying muscle tissue.

To expand our understanding of oligothiophene-containing coordination complexes, we are examining variations in their central metals, coordinating ligands, thienyl groups, counterions, and coordination geometries.[11,14,17,20,46,49−51] We aim to establish structure−activity relationships (SARs) for medicinally active complexes that reconcile their physicochemical, photophysical, electrochemical, and biological properties with the ideal phototherapy profile for a given clinical setting. In this study we introduce a series of Ru(II) PSs (**Ru-*n*T**), each featuring two 4,4′-bis(trifluoromethyl)-2,2′-bipyridine (4,4′-btfmb) coligands and a thienyl-containing imidazo[4,5-*f*][1,10]phenanthroline (IP-*n*T) ligand with n = 1−4 thiophene rings. The members are compared to the parent $[Ru(4,4'\text{-btfmb})_2(LL)]^{2+}$ complexes with LL = IP-0T, 1,10-phenanthroline (phen), or 4,4′-btfmb (Chart 1b). The syntheses and structural characterization of complexes **Ru-3T** and **Ru-4T** were previously published.[52,53] In this study, the photocytotoxic effects of $[Ru(4,4'\text{-btfmb})_2(\text{IP-}n\text{T})]^{2+}$ (n = 1−4) and the parent complexes without *n*T groups are examined on melanoma cells under various light conditions and oxygen levels. We also report on their lipophilicities, steady-state absorption and emission characteristics, excited-state properties, electronic configurations, and electrochemical profiles.

2. MATERIALS AND METHODS

The complexes in this series were characterized by ^{1}H NMR, high-performance liquid chromatography (HPLC), and ESI$^+$ mass spectrometry (MS). They were evaluated for lipophilicity, ground and excited-state characteristics using absorption and emission spectroscopy, electrochemistry, and (photo)cytotoxicity. Further details regarding procedures and characterization data are available in the Supporting Information (SI).

2.1. Instrumentation. A CEM Discover microwave reactor was used to perform microwave reactions. Flash column chromatography was carried out on the Teledyne ISCO EZ Prep UV model of CombiFlash EZ Prep using SILICYCLE SiliaSep 25 g prepacked silica cartridges. Size-exclusion chromatography was performed using a gravity column packed with Sephadex LH-20. The NMR spectra were collected on JEOL 500 MHz spectrometers (University of North Carolina at Greensboro, University of Texas at Arlington) operating at 500 MHz for ^{1}H experiments, and on an Agilent 700 MHz Magnet spectrometer (The Joint School of Nanoscience and Nanoengineering at Greensboro) operating at 700 MHz for ^{1}H experiments. The chemical shifts are reported in parts per million (ppm) and were referenced to the residual solvent peaks. High-resolution ESI$^+$ mass spectra were obtained using a Thermo Fisher Scientific LTQ Orbitrap XL instrument (Triad Mass Spectrometry Laboratory at University of North Carolina at Greensboro) and Shimadzu IT-TOF instrument (Shimadzu Center for Advanced Analytical Chemistry at University of Texas at Arlington). HPLC analyses were carried out on an Agilent/Hewlett-Packard 1100 series instrument in 100 μM solutions in methanol using a Hypersil GOLD C18 reversed-phase column with an A → B gradient (98% → 5% A; A = 0.1% formic acid in H_2O, B = 0.1% formic acid in MeCN). Reported retention times are accurate to within ±0.1 min.

2.2. Synthesis and Characterization. We previously published the synthetic methods and structural characterization of **Ru-3T** and **Ru-4T**,[52,53] and $[Ru(4,4'\text{-btfmb})_3]^{2+}$ has been reported by others.[54−57] To the best of our knowledge, all other complexes presented in this study have not been reported. All complexes were prepared as racemic mixtures. Solvents and reagents were purchased from commercial sources and used without further purification. Water used for all biological experiments was deionized to a resistivity ≥ 18.2 MΩ using either a Barnstead or Milli-Q filtration system. Methanol was purchased from Fisher Scientific (ACS grade for synthesis, HPLC grade for LC eluent, Optima grade for HPLC and MS sample preparation). Deuterated solvents for NMR were purchased from Cambridge Isotope Laboratories. Ruthenium(III) trichloride trihydrate was purchased from Ark Pharm and Acros Organics. $Ru(4,4'\text{-btfmb})_2Cl_2\cdot 2H_2O$[58] and IP-based ligands[59] were prepared according to adapted literature procedures. The synthesis of IP-based ligands follows that described below for IP-4T.

https://doi.org/10.1021/acs.inorgchem.3c04382
Inorg. Chem. XXXX, XXX, XXX−XXX

[2,2′:5′,2″:5″,2‴-Quaterthiophene]-5-carbaldehyde (4T-CHO) was prepared as previously described.[60,61] The final products are synthetically characterized in Figures S1−S21 via ^{1}H NMR, ^{1}H−^{1}H COSY NMR, HPLC, and ESI$^+$-MS. The Cl^- salts of final complex products were obtained via anion metathesis on HCl-treated Amberlite IRA-410 resin with methanol as the eluent and isolated in vacuo. Final complexes are a mixture of Δ/Λ isomers.

2.2.1. rac-[Ru(4,4′-btfmb)$_3$](Cl)$_2$. Ru(Cl)$_3$·xH$_2$O (58 mg, 0.2 mmol) and 4,4′-btfmb (175 mg, 0.6 mmol) were added to a microwave vessel containing argon-purged ethylene glycol (3 mL), and then the mixture was subject to microwave irradiation at 180 °C for 45 min with stirring. The resulting dark red solution was then transferred to a separatory funnel with deionized water (25 mL) and CH_2Cl_2 (25 mL). After gentle agitation, CH_2Cl_2 was drained and the remaining aqueous layer was washed with CH_2Cl_2 (25 mL) until the CH_2Cl_2 layer was colorless. Then, CH_2Cl_2 (25 mL) and saturated aqueous KPF_6 (5 mL) were added, and the mixture was shaken gently. The CH_2Cl_2 layer was drained and the product was further extracted from the aqueous layer with CH_2Cl_2 (25 mL) until the aqueous layer was colorless. The CH_2Cl_2 extracts were then combined and concentrated under reduced pressure. The crude product was then purified using silica gel flash column chromatography with a gradient of MeCN to 10% water in MeCN, followed by 7.5% water in MeCN with 0.5% KNO_3. The product-containing fractions were then combined and concentrated under vacuum, then transferred to a separatory funnel with CH_2Cl_2 (25 mL), deionized water (25 mL), and saturated aqueous KPF_6 (1 mL). The resulting mixture was gently agitated and the CH_2Cl_2 layer was drained. Additional CH_2Cl_2 (25 mL) was used to extract the remaining product until the aqueous layer was colorless. The CH_2Cl_2 layers were then combined and dried under vacuum. This was then converted to the corresponding Cl^- salt in quantitative yield using Amberlite IRA-410 with MeOH as the eluent, then purifying further using Sephadex LH-20 with MeOH as the eluent, affording a dark red solid (50 mg, 20%). ^{1}H NMR (400 MHz, MeOD-d_3, ppm): δ 9.41 (d, J = 1.9 Hz, 6H), 8.15 (d, J = 5.9 Hz, 6H), 7.86 (dd,J = 6.0, 1.8 Hz, 6H). HRMS (ESI+) m/z for $[M-2Cl^-]^{2+}$ calcd: 489.0169; found: 488.9529. HPLC retention time: 22.41 min (99.5% purity by peak area).

*2.2.2. rac-[Ru(4,4′-btfmb)$_2$(phen)](Cl)$_2$ (**Ru-phen**).* Ru(4,4′-btfmb)$_2$Cl$_2$·2H$_2$O (91 mg, 0.12 mmol) and phen (22 mg, 0.1 mmol) were added to a microwave vessel containing argon-purged ethylene glycol (4 mL) and subjected to microwave irradiation at 180 °C for 15 min. The resulting dark red mixture was then isolated and purified in the same manner as [Ru(4,4′-btfmb)$_3$](Cl)$_2$, yielding the desired product as a dark red solid (43 mg, 45%). ^{1}H NMR (400 MHz, MeOD-d_3, ppm): δ 9.38 (d, J = 14.1 Hz, 4H), 8.81 (d, J = 8.0 Hz, 2H), 8.36 (s, 2H), 8.28 (d, J = 5.9 Hz, 2H), 8.23 (d, J = 5.3 Hz, 2H), 7.94−7.84 (m, 6H), 7.67 (dd, J = 6.0, 1.8 Hz, 2H). HRMS (ESI+) m/z for $[M-2Cl^-]^{2+}$ calcd: 433.0295; found: 432.9739. HPLC retention time: 22.41 min (99.5% purity by peak area).

*2.2.3. rac-[Ru(4,4′-btfmb)$_2$(IP)](Cl)$_2$ (**Ru-0T**).* Ru(4,4′-btfmb)$_2$Cl$_2$·2H$_2$O (91 mg, 0.12 mmol) and IP (22 mg, 0.1 mmol) were added to a microwave vessel containing argon-purged ethylene glycol (4 mL) and subjected to microwave irradiation at 180 °C for 15 min. The resulting dark red mixture was then isolated and purified in the same manner as [Ru(4,4′-btfmb)$_3$](Cl)$_2$, yielding the desired product as a dark red solid (81.3 mg, 51%). ^{1}H NMR (400 MHz, MeOD-d_3, ppm): δ 9.38 (dd, J = 16.6, 1.9 Hz, 4H), 9.10 (d, J = 8.4 Hz, 2H), 8.68 (s, 1H), 8.29 (d, J = 5.9 Hz, 2H), 8.15 (dd, J = 5.3, 1.3 Hz, 2H), 7.95 (d, J = 6.0 Hz, 2H), 7.92 (dd, J = 8.3, 5.3 Hz, 2H), 7.87 (dd, J = 6.0, 1.9 Hz, 2H), 7.66 (dd, J = 6.0, 1.9 Hz, 2H). HRMS (ESI+) m/z for $[M-2Cl^-]^{2+}$ calcd: 453.0326; found: 452.9735. HPLC retention time: 20.33 min (>98% purity by peak area).

*2.2.4. rac-[Ru(4,4′-btfmb)$_2$(IP-1T)](Cl)$_2$ (**Ru-1T**).* Ru(4,4′-btfmb)$_2$Cl$_2$·2H$_2$O (91 mg, 0.12 mmol) and IP-1T (30 mg, 0.1 mmol) were added to a microwave vessel containing ethylene glycol (4 mL) and subjected to microwave irradiation at 180 °C for 15 min. The dark red solution was transferred to a separatory funnel with H$_2$O (25 mL) and CH_2Cl_2 (25 mL). CH_2Cl_2 layer was used to wash the aqueous layer. CH_2Cl_2 (25 mL) and saturated aqueous KPF_6 (5 mL) were used to extract the product from the aqueous layer. The product was then purified using silica gel flash column chromatography. The product-containing fractions were transferred to a separatory funnel with CH_2Cl_2 (25 mL), H$_2$O (25 mL), and saturated aqueous KPF_6 (1 mL) and the [Ru(4,4′-btfmb)$_2$(IP-1T)](PF$_6$)$_2$ product was isolated via extraction. The PF_6^- salt was then converted to the corresponding Cl^- salt in quantitative yield using Amberlite IRA-410 with MeOH as the eluent, followed by further purification using Sephadex LH-20 with MeOH as the eluent, yielding [Ru(4,4′-btfmb)$_2$(IP-1T)](Cl)$_2$ as a dark red solid (43 mg, 25%). ^{1}H NMR (400 MHz, MeOD-d_3, ppm): δ 9.40 (d, J = 1.9 Hz, 2H), 9.36 (d, J = 1.8 Hz, 2H), 9.19 (s, 2H), 8.29 (d, J = 5.8 Hz, 2H), 8.12 (d, J = 5.2 Hz, 2H), 8.01 (d, J = 3.6 Hz, 1H), 7.97 (d, J = 6.1 Hz, 2H), 7.91 (dd, J = 8.3, 5.2 Hz, 2H), 7.88 (dd, J = 6.0, 1.9 Hz, 2H), 7.74 (d, J = 5.0 Hz, 1H), 7.68 (dd, J = 6.1, 1.8 Hz, 2H), 7.31 (dd, J = 5.0, 3.7 Hz, 1H). HRMS (ESI+) m/z for $[M-2Cl-H]^+$ calcd: 494.0265; found: 494.0261, m/z for $[M-2Cl-H]^+$ calcd: 987.0456; found: 987.0474. HPLC retention time: 21.75 min (99% purity by peak area).

*2.2.5. rac-[Ru(4,4′-btfmb)$_2$(IP-2T)](Cl)$_2$ (**Ru-2T**).* Ru(4,4′-btfmb)$_2$Cl$_2$·2H$_2$O (91 mg, 0.12 mmol) and IP-2T (38 mg, 0.1 mmol) were added to a microwave vessel containing argon-purged ethylene glycol (4 mL) and subjected to microwave irradiation at 180 °C for 15 min. The resulting dark red mixture was then isolated and purified in the same manner as **Ru-1T**, yielding the desired product as a dark solid (33 mg, 29%). ^{1}H NMR (400 MHz, MeOD-d_3, ppm): δ 9.40 (d, J = 1.9 Hz, 2H), 9.37 (d, J = 1.9 Hz, 2H), 9.17 (s, 2H), 8.29 (d, J = 5.8 Hz, 2H), 8.13 (dd, J = 5.2, 1.2 Hz, 2H), 7.99 (d, J = 6.1 Hz, 2H), 7.94 (d, J = 3.8 Hz, 1H), 7.91 (dd, J = 8.3, 5.2 Hz, 2H), 7.88 (dd, J = 5.9, 1.9 Hz, 2H), 7.71−7.67 (m, 2H), 7.47 (dd, J = 5.1, 1.1 Hz, 1H), 7.43−7.38 (m, 2H), 7.13 (dd, J = 5.1, 3.6 Hz, 1H). HRMS (ESI+) m/z for $[M-2Cl^-]^{2+}$ calcd: 535.0203; found: 535.0201, m/z for $[M-2Cl^--H]^+$ calcd: 1069.0333; found: 1069.0353. HPLC retention time: 22.86 min (95.2% purity by peak area).

*2.2.6. rac-[Ru(4,4′-btfmb)$_2$(IP-3T)](Cl)$_2$ (**Ru-3T**).* Ru(4,4′-btfmb)$_2$Cl$_2$·2H$_2$O (151 mg, 0.2 mmol) and IP-3T (76 mg, 0.164 mmol) were added to a microwave vessel containing argon-purged ethylene glycol (4 mL) and subjected to microwave irradiation at 180 °C for 15 min. The resulting dark red mixture was then isolated and purified in the same manner as **Ru-1T**, yielding the desired product as a dark red solid (55 mg, 27%). ^{1}H NMR (700 MHz, MeOD-d_3, ppm): δ 9.40 (d, J = 2.0 Hz, 2H), 9.37 (d, J = 1.9 Hz, 2H), 9.26 (s, 1H), 9.11 (s, 1H), 8.29 (d, J = 5.8 Hz, 2H), 8.14 (dd, J = 5.2, 1.3 Hz, 2H), 7.99 (s, 2H), 7.95−7.90 (m, 3H), 7.88 (dd, J = 6.0, 1.9 Hz, 2H), 7.69 (dd, J = 6.1, 1.9 Hz, 2H), 7.40 (d, J = 3.8 Hz, 1H), 7.35 (d, J = 3.8 Hz, 1H), 7.31 (dd, J = 3.5, 1.1 Hz, 1H), 7.23 (d, J = 3.8 Hz, 1H), 7.09 (dd, J = 5.1, 3.6 Hz, 1H). ^{13}C NMR (700 MHz, MeOD-d_3, ppm): δ 163.28, 163.08, 162.89, 159.60, 159.43, 155.07, 154.53, 150.34, 141.88, 140.97, 140.81, 140.77, 140.60, 139.10, 137.67, 135.97, 131.57, 129.82, 129.20, 126.94, 126.39, 125.84, 125.75, 125.40, 125.33, 125.23, 124.45, 124.34, 123.11, 123.02, 122.89, 122.79, 119.88. HRMS (ESI+) m/z for $[M-2Cl^-]^{2+}$ calcd: 576.0142; found: 576.0141, m/z for $[M-2Cl^--H]^+$ calcd: 1151.0211; found: 1151.0232. HPLC retention time: 23.80 min (95.4% purity by peak area).

*2.2.7. rac-[Ru(4,4′-btfmb)$_2$(IP-4T)](Cl)$_2$ (**Ru-4T**).* Ru(4,4′-btfmb)$_2$Cl$_2$·2H$_2$O (114 mg, 0.2 mmol) and IP-4T (90 mg, 0.164 mmol) were added to a microwave vessel containing argon-purged ethylene glycol (4 mL) and subjected to microwave irradiation at 180 °C for 15 min. The reaction mixture was transferred to a 100 mL beaker and diluted with ∼30 mL of H$_2$O, then treated with 3 mL of saturated aqueous KPF_6, and stirred for 5 min. At this time, a red precipitate formed and was collected using a Büchner filtration apparatus. The product was then purified following the same procedure as described for **Ru-1T**, yielding [Ru(4,4′-btfmb)$_2$(IP-4T)](Cl)$_2$ as a dark red solid (77 mg, 35%). ^{1}H NMR (700 MHz, MeOD-d_3, ppm): δ 9.40 (d, J = 2.0 Hz, 2H), 9.37 (d, J = 1.9 Hz, 2H), 9.26 (s, 1H), 9.11 (s, 1H), 8.29 (d, J = 5.8 Hz, 2H), 8.14 (dd, J = 5.2, 1.3 Hz, 2H), 7.99 (s, 2H), 7.95−7.90 (m, 3H), 7.88 (dd, J = 6.0, 1.9 Hz, 2H), 7.69 (dd, J = 6.1, 1.9 Hz, 2H), 7.40 (d, J = 3.8 Hz, 1H), 7.35 (d, J = 3.8 Hz, 1H), 7.31 (dd, J = 3.5, 1.1 Hz, 1H), 7.23 (d, J = 3.8 Hz,

https://doi.org/10.1021/acs.inorgchem.3c04382
Inorg. Chem. XXXX, XXX, XXX−XXX

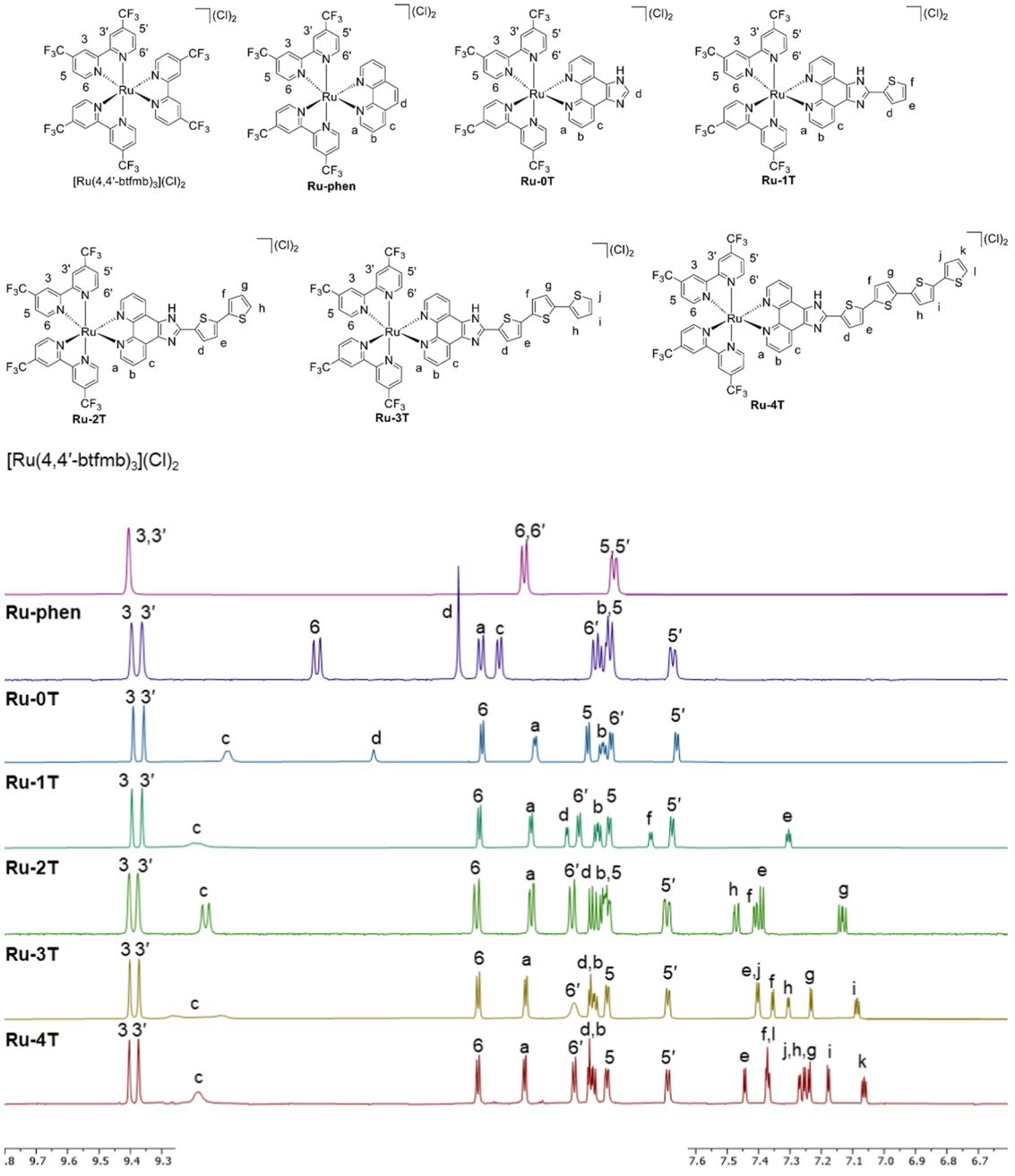

Figure 1. ^{1}H NMR spectra showing the aromatic region for $[Ru(4,4'\text{-btfmb})_3](Cl)_2$ and **Ru-*n*T** (n = 0−4) in MeOD-d_3 (Cl^- salts; 298 K). All spectra were collected at 500 MHz, except for **Ru-4T**, which was collected at 700 MHz.

1H), 7.09 (dd, J = 5.1, 3.6 Hz, 1H). ^{13}C NMR (175 MHz, MeOD-d_3, ppm): δ 163.28, 163.08, 162.89, 159.60, 159.43, 155.07, 154.53, 150.34, 141.88, 140.97, 140.81, 140.77, 140.60, 139.10, 137.67, 135.97, 131.57, 129.82, 129.20, 126.94, 126.39, 125.84, 125.75, 125.40, 125.33, 125.23, 124.45, 124.34, 123.11, 123.02, 122.89, 122.79, 119.88. HRMS (ESI+) m/z for $[M-2Cl]^{2+}$ calcd for $C_{49}H_{26}F_{12}N_8RuS_3$: 576.0142; found: 576.0141. $[M-2Cl-H]^+$ calcd for $C_{49}H_{25}F_{12}N_8RuS_3$: 1151.0211; found: 1151.0232. HPLC retention time: 23.80 min (99% purity by peak area).

2.3. Computational Details. The complexes of this series were studied with a combination of density functional theory (DFT) and time-dependent density functional theory (TDDFT) methods[62] as implemented in the Gaussian 16 software.[63] This computational protocol has been used to describe a variety of metal complex PSs for PDT, including Ru(II) and Os(II) systems.[17,46,49,51,64−71] The geometries of the lowest-energy singlet and triplet excited states were optimized with the PBE0 exchange-correlation functional[72] combined with the 6-31+G(d,p) basis set for all atoms except Ru, which was described with the Stuttgart−Dresden pseudopotential.[73] The M06 exchange-correlation functional was used to compute the electronic excited states on top of the optimized geometries through the TDDFT formalism, making use of the Tamm−Dancoff approximation (TDA).[74] This level of theory has been employed recently to describe ^{3}MLCT and ^{3}ILCT/^{3}LLCT excited states and to predict emission energies for related oligothiophene-based Ru(II) and Os(II) complexes, providing a more accurate description of the vertical triplet-state energies with respect to the conventional TDDFT analysis (which tends to underestimate the energy gaps[75]). The calculations were performed in water within the framework of the integral equation formalism polarizable continuum model (IEFPCM),[76−78] with the dielectric constant of ε = 80 and default Gaussian 16 parameters. The excited-state topologies were analyzed

https://doi.org/10.1021/acs.inorgchem.3c04382
Inorg. Chem. XXXX, XXX, XXX−XXX

by postprocessing of the Gaussian 16 output in two ways: (i) determination of the natural transition orbitals (NTOs) with the Chemissian 4.67 software[79] and (ii) computation of the charge-transfer descriptors through fragment-based analyses performed with the TheoDORE 3.1.1 toolbox.[80]

2.4. Electrochemistry. Voltammetry was performed in dimethylformamide (DMF, Fisher HPLC grade) that had been dried and deoxygenated with an Inert PureSolv MD7 solvent purification system, with 100 mM tetrabutylammonium hexafluorophosphate ($TBAPF_6$) (Fisher) as the supporting electrolyte, in a two-compartment low-volume cell with the three-electrode configuration under argon. A 3 mm glassy carbon disc was used as the working electrode with a platinum wire counter electrode and a Ag/AgCl/4 M KCl reference electrode. Ferrocene (Fc) was used as an internal standard. The complex solutions were approximately 4 mM for oxidation sweeps and 0.25 mM for reduction sweeps.

Measurements were conducted at room temperature using a WaveNow potentiostat (Pine Research Company) with Aftermath software. Cyclic differential pulse voltammetry (CDPV) measurements used a sweep rate of 2 $mV{\cdot}s^{-1}$ with a modulation amplitude varying from 12.5 to 100 mV. For reversible processes, the formal redox potential $E^{o\prime}$ was taken as the average of E_{pa} (anodic peak potential) and E_{pc} (cathodic peak potential). For quasi-reversible processes, only E_{pa} or E_{pc} is reported.

3. RESULTS AND DISCUSSION

3.1. Synthesis and Characterization. $[Ru(4,4'\text{-btfmb})_3]^{2+}$ and **Ru-*n*T** were synthesized utilizing our established method for related Ru(II) 2,9-dimethyl-1,10-phenanthroline systems.[17] The initially isolated PF_6^- salts of the complexes were purified using silica gel flash chromatography and then converted to their corresponding Cl^- salts on Amberlite IRA-410. Then, size-exclusion chromatography was carried out on Sephadex LH-20 to give final yields of approximately 60% for $[Ru(4,4'\text{-btfmb})_3]^{2+}$, **Ru-0T**, **Ru-1T**, and **Ru-3T**, around 40% for **Ru-2T**, and close to 30% for **Ru-4T**. These complexes underwent thorough characterization by 1D and 2D ^1H NMR spectroscopy (Figures 1 and S1−S7), with signal assignments for $[Ru(4,4'\text{-btfmb})_3]^{2+}$ and **Ru-0T**−**Ru-4T** conducted using $^1H-^1H$ COSY NMR. The assignments aligned with those of our previously reported, related compounds.[17,20,46] Additionally, these complexes were characterized by high-resolution ESI^+ MS (Figures S8−S14). The complexes were ≥95% pure by HPLC (Figures S15−S21).

The lipophilicities of the chloride salts of complexes were determined by measuring their distribution between 1-octanol and 10 mM phosphate buffer (pH 7.4) following the "shake-flask" method as we described previously.[49] The $\log D_{o/w}$ values for this series span 4 orders of magnitude, with $[Ru(4,4'\text{-btfmb})_3]^{2+}$ being the most hydrophilic at about −2 and **Ru-4T** most lipophilic near +2 (Figure 2). The three reference compounds lacking thiophene rings ($[Ru(4,4'\text{-btfmb})_3]^{2+}$, **Ru-phen**, and **Ru-0T**) as well as **Ru-1T** show a preference for the aqueous buffer and accordingly have negative $\log D_{o/w}$ values. In contrast, complexes with 2−4 thiophenes (**Ru-2T**, **Ru-3T**, **Ru-4T**) have positive $\log D_{o/w}$ values and increase on going from n = 2 to 4. The addition of the trifluoromethyl group qualitatively improved the overall aqueous solubility of the complexes with positive $\log D_{o/w}$ values compared to analogous Ru(II) and Os(II) complexes with other coligands where 4T often leads to precipitation at the octanol/buffer interface.[46,49]

3.2. Computation. *3.2.1. Singlet States.* The singlet ground-state structures for $[Ru(4,4'\text{-btfmb})_3]^{2+}$, **Ru-phen**, and **Ru-*n*T** (n = 0−4) optimized in water at the DFT/PBE0 level of theory are shown in Figure 3. The associated geometric parameters (Table S3) confirm the octahedral arrangement of coordinating nitrogen atoms around the central Ru(II) ion and similar Ru−N bond distances for all of the compounds. The thiophene ring of **Ru-1T** and the first thiophene ring of **Ru-*n*T** (n = 2−4) are coplanar with the coordinating IP ligand, but additional thienyl rings are conformationally more flexible. In the case of **Ru-4T**, the fourth thiophene ring is twisted as much as 18° with respect to the IP plane.

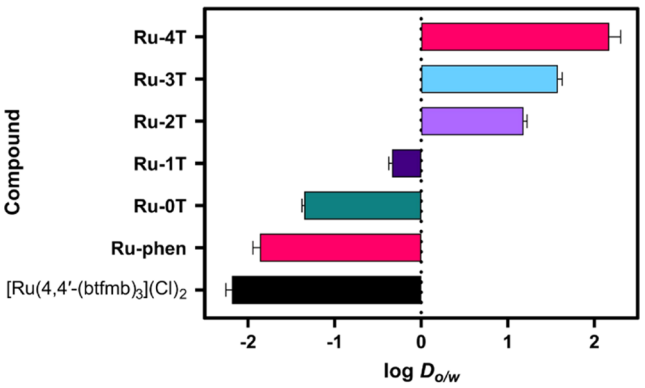

Figure 2. Lipophilicities of $[Ru(4,4'\text{-btfmb})_3](Cl)_2$, **Ru-phen**, and **Ru-*n*T** (n = 0−4) in 1-octanol and phosphate buffer using the in-house "shake-flask" method.

The nT chain length impacts the frontier molecular orbitals and the resulting electronic transitions. The systematic reduction of the highest occupied molecular orbital (HOMO)−lowest unoccupied molecular orbital (LUMO) gaps with longer thiophene chains is due to an increase in the HOMO energies as the orbital contribution from nT increases. The LUMOs are primarily bftmb-based (>70%) with similar energies across the series, but the nT contribution to the HOMO reaches 51% for **Ru-3T** and almost 66% for **Ru-4T** (Figures 4 and S22, Table S4). The red shift of the lowest-energy spin-allowed singlet−singlet electronic transitions with increasing n is accompanied by a change in the nature of these states toward mixed ^{1}LLCT/^{1}ILCT/^{1}IL character for n > 2 as shown by the natural transition orbital (NTO) analysis (Figures 5 and S23), consistent with other oligothiophene-bearing Ru(II) and Os(II) complexes.[17,20,46,51,67] The NTOs are predominantly ^{1}MLCT (Ru → 4,4′-btfmb) for the complexes lacking thiophene rings and **Ru-1T**, with electronic transitions computed in the range of 438−459 nm (only slightly higher in energy than the experimental bands falling between 456 and 471 nm in Figure 3). The NTOs for **Ru-2T** are of mixed ^{1}MLCT (53%)/^{1}LLCT (26%) character (^{1}LLCT is nT → 4,4′-btfmb), and the lowest-energy transition is computed at 455 nm in close agreement with the experimental band at 462 nm. In contrast, the NTOs for **Ru-3T** and **Ru-4T** lack ^{1}MLCT character and are mixed ^{1}LLCT/^{1}ILCT/^{1}IL. Both complexes have lowest-energy transitions with significant ^{1}LLCT (nT → IP) character (55% for **Ru-3T** and 45% for **Ru-4T**) but differ in the relative contributions of ^{1}ILCT versus ^{1}IL. The NTOs for **Ru-3T** have a larger contribution from ^{1}IL (IP-based $\pi\pi^*$) compared to ^{1}ILCT (nT-based CT). The opposite is true for **Ru-4T**, where the ^{1}ILCT contribution is slightly more than that of ^{1}IL. The computed transitions are 469 and 493 nm for **Ru-3T** and **Ru-4T**, respectively, which lie within the broadened spectral features in the experimental spectra.

https://doi.org/10.1021/acs.inorgchem.3c04382
Inorg. Chem. XXXX, XXX, XXX−XXX

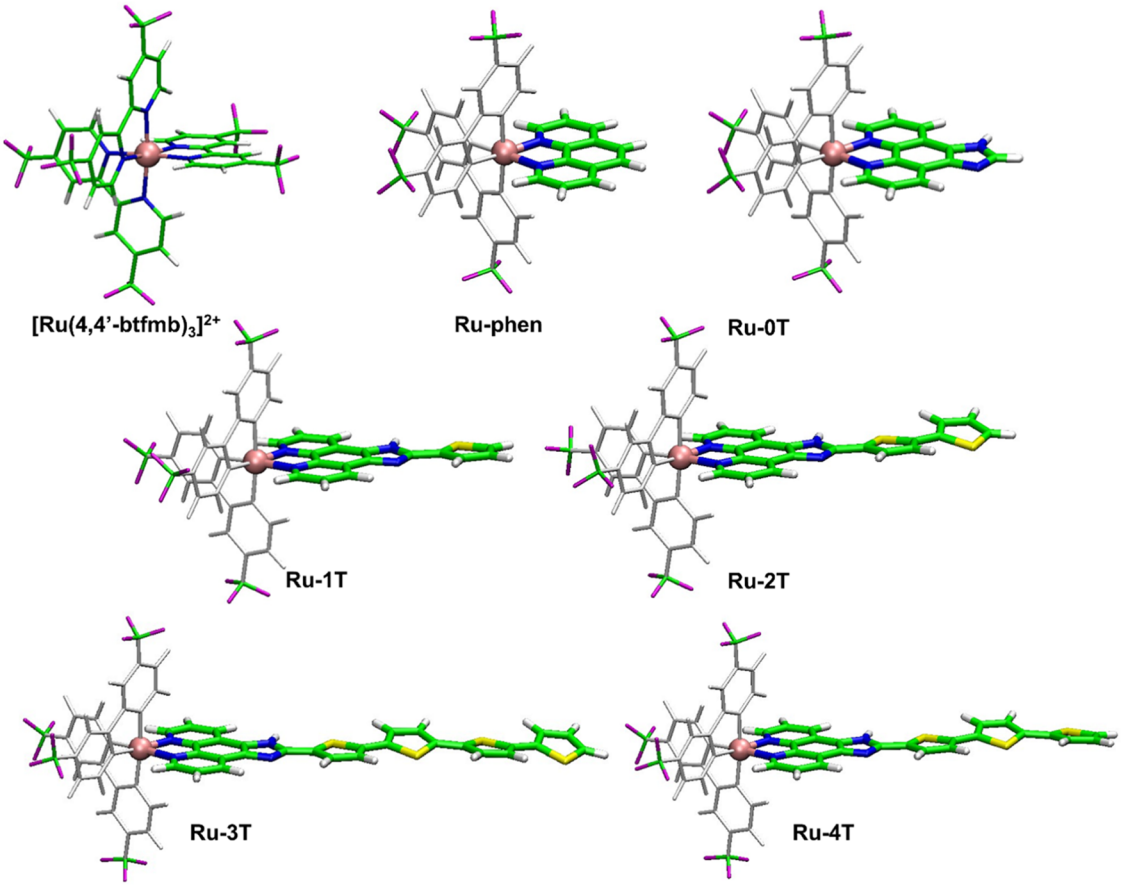

Figure 3. Optimized geometries of $[Ru(4,4'\text{-btfmb})_3]^{2+}$, **Ru-phen**, and **Ru-*n*T** (n = 0−4) in a water environment at the PBE0/6-31+G(d,p)/SDD level of theory. For the sake of clarity, the 4,4′-btfmb coligands are shown in gray for all of the complexes except for $[Ru(4,4'\text{-btfmb})_3]^{2+}$.

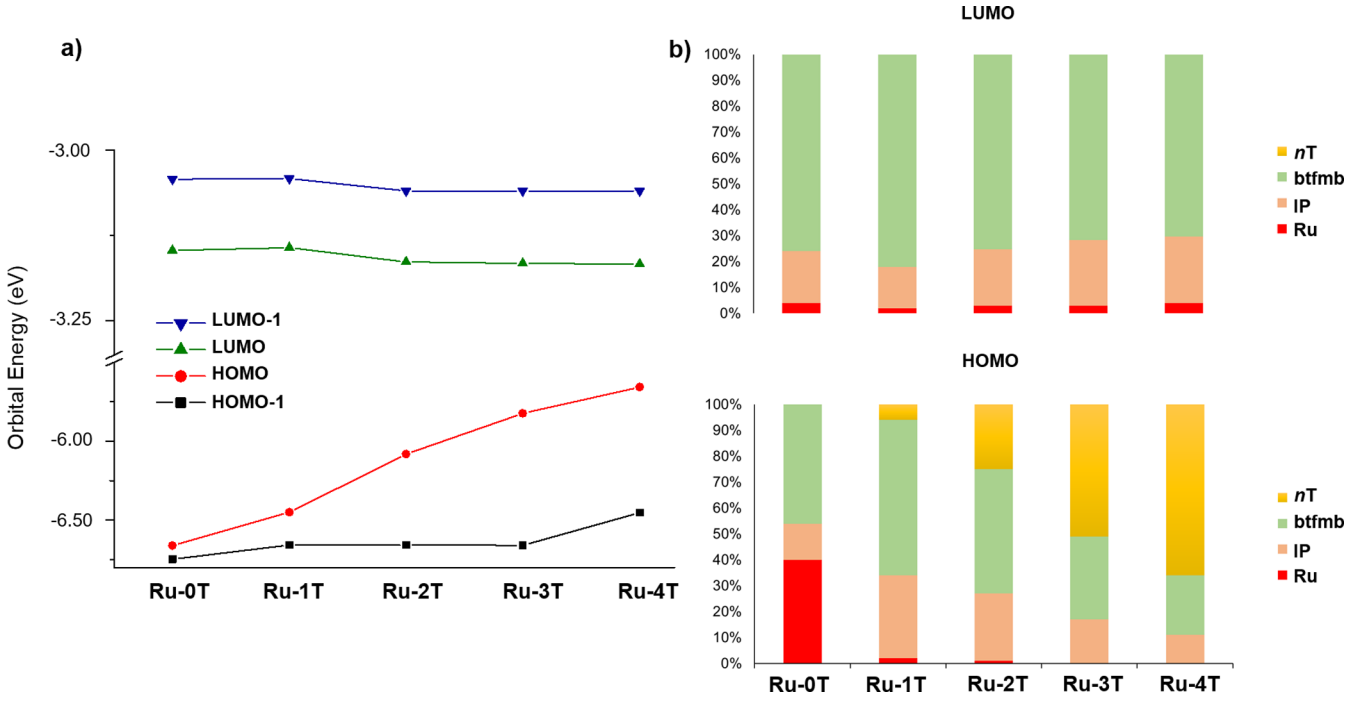

Figure 4. (a) Calculated HOMO, LUMO, HOMO−1 and LUMO+1 orbital energies. (b) Percent contribution of the nT, bftmb, IP, and Ru fragments to the HOMO and LUMO orbitals, for **Ru-*n*T** (n = 0−4) in the singlet ground state, at the M06/6-31+G(d,p)/SDD level of theory. Additional details can be found in the Supporting Information.

https://doi.org/10.1021/acs.inorgchem.3c04382
Inorg. Chem. XXXX, XXX, XXX−XXX

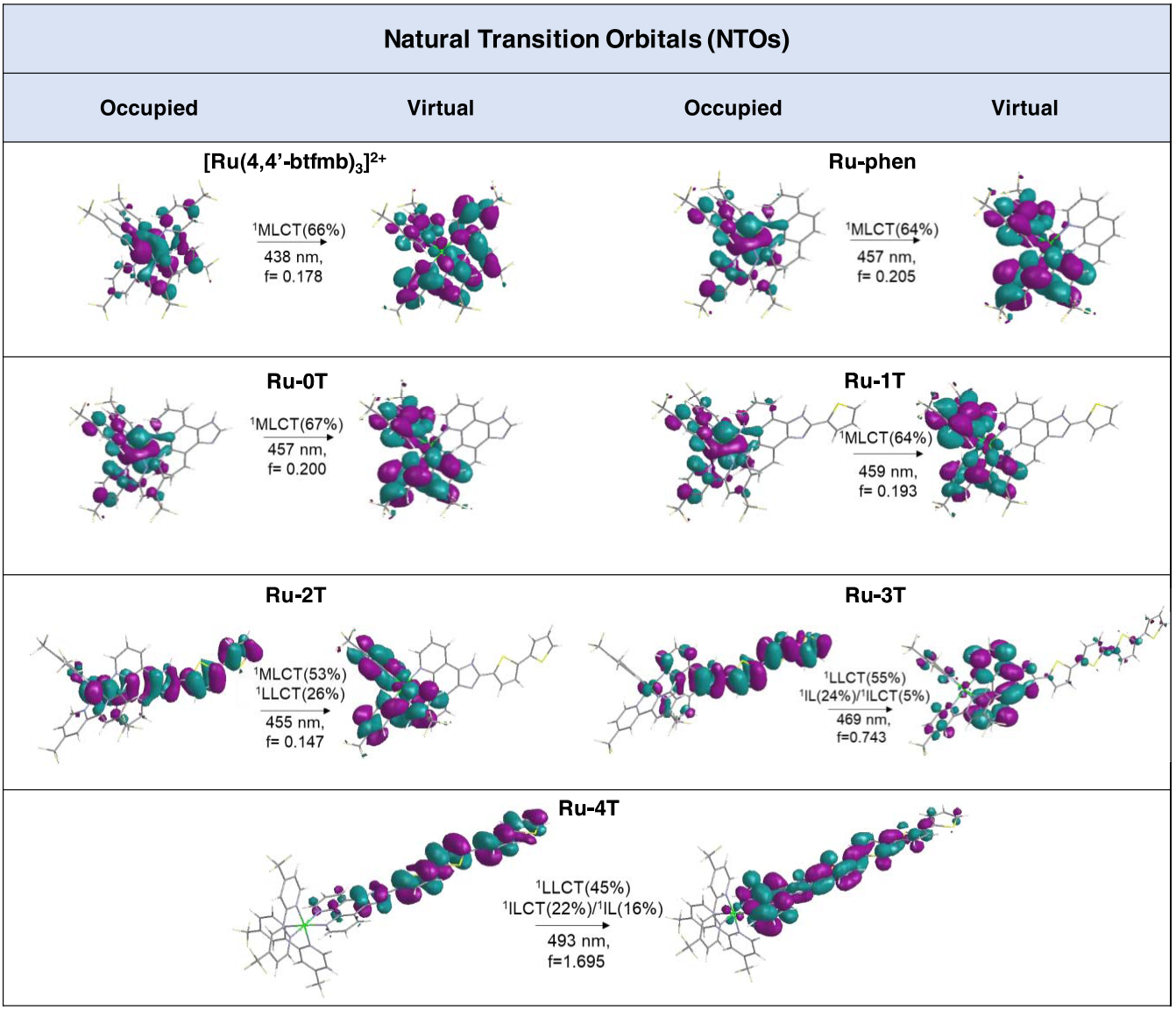

Figure 5. Occupied and virtual NTOs of the computed lowest-energy singlet−singlet transitions in water (λ) with the predominant character indicated. Additional NTOs are reported in Figure S23.

3.2.2. Triplet States. The lowest-energy excited triplet-state (T_1) structures for $[Ru(4,4'\text{-btfmb})_3]^{2+}$, **Ru-phen**, and **Ru-*n*T** are similar to their corresponding ground-state structures except that those involving oligothiophenes adopt a completely planar chain conformation for maximum π-conjugation, with successive *n*T groups antiplanar with respect to one another. The geometrical parameters of these optimized T_1 states are compiled in Table S3 alongside the data for S_0. All complexes, with the exception of **Ru-3T** and **Ru-4T**, have T_1 states that are ^{3}MLCT (Ru → btfmb), as shown by the NTO analyses (Figures 6 and S24, Table 1) and supported by Mulliken spin densities (MSDs) close to 1 for the Ru(II) center (Table S3). In sharp contrast, T_1 is localized primarily to the IP-*n*T ligand for **Ru-3T** and **Ru-4T** and its nature changes to mixed ^{3}ILCT/^{3}LLCT/^{3}IL. The largest contributor to these mixed T_1 states is ^{3}ILCT (CT within the *n*T chain) and is slightly more for **Ru-4T** (51 vs 39%), whereas the ^{3}IL contribution (*n*T-localized) is similar for both at ∼20% and ^{3}LLCT (CT from *n*T to IP) contributes more for **Ru-3T** (25%) and less for **Ru-4T** (16%). The ^{3}MC states involving Ru(II) and ^{3}IL states localized to 4,4′-btfmb or IP are higher in energy and do not contribute to the computed NTOs for the lower-energy excited states.

The computed adiabatic ^{3}MLCT energies lie near 1.9−2.0 eV across the series, regardless of whether this state is T_1 or T_2 (Tables 1 and S5). These ^{3}MLCT energies are lower (by ∼0.2 to 0.3 eV) than those for related Ru(II) polypyridyl systems without substituted ligands due to the electron-withdrawing groups of the 4,4′-btfmb coligands in this series. These groups do not impact the ^{3}ILCT/^{3}LLCT/^{3}IL energies, which are very similar to those computed for the related series with 1,10-phenanthroline (phen) coligands.[51] However, the lower ^{3}MLCT energies in the Ru(II) 4,4′-btfmb complexes result in an ^{3}MLCT-based T_1 for **Ru-2T** (rather than the IP-*n*T-based triplet that tends to be T_1 in other related families). The mixed ^{3}ILCT/^{3}LLCT/^{3}IL states that are T_1 in the case of **Ru-3T** and **Ru-4T** have computed adiabatic energies of 1.54 and 1.42 eV, respectively. The drop in energy of the T_1 state for **Ru-3T** and **Ru-4T** is directly related to its organic ^{3}ILCT

https://doi.org/10.1021/acs.inorgchem.3c04382
Inorg. Chem. XXXX, XXX, XXX−XXX

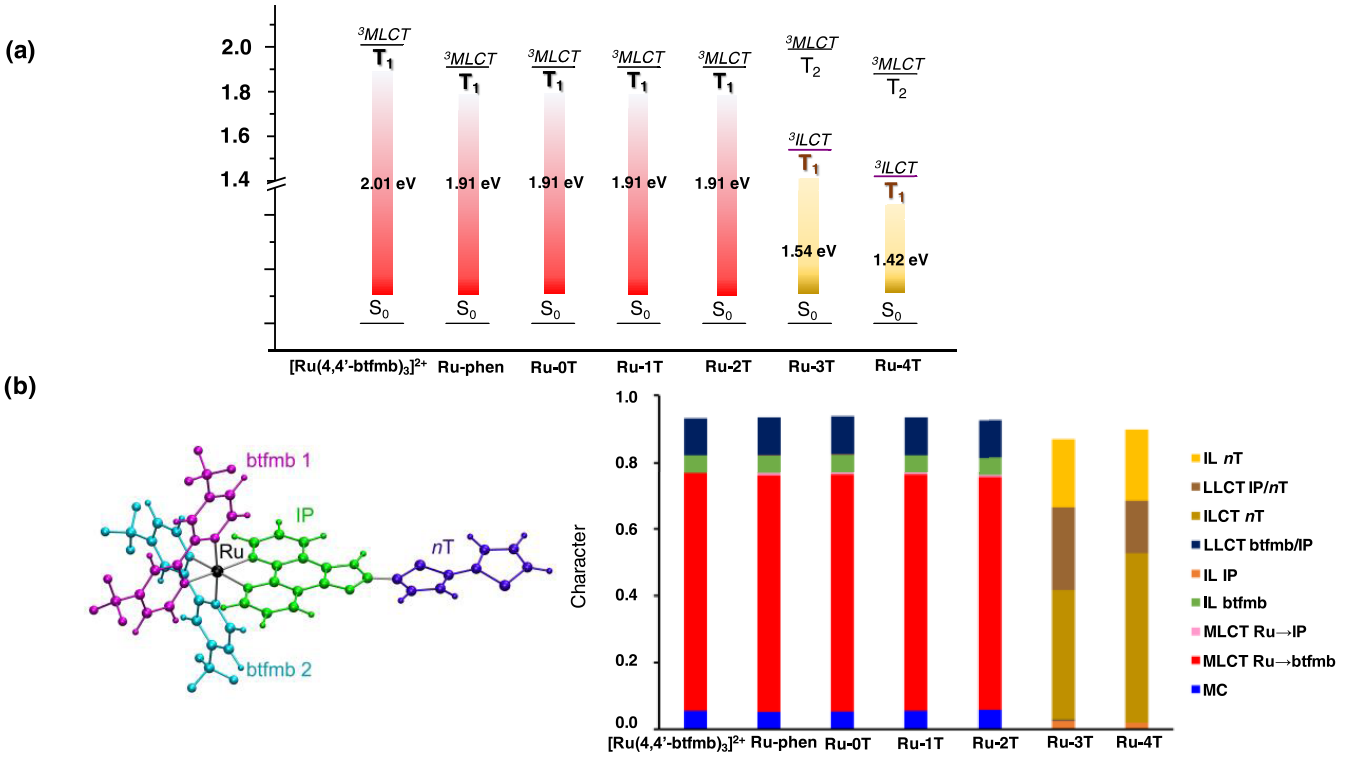

Figure 6. (a) Computed T_1 adiabatic energies for $[Ru(4,4'\text{-btfmb})_3]^{2+}$, **Ru-phen**, and **Ru-*n*T** (n = 0−4). (b) Molecular fragments (left) defined to quantify the molecular topology of the T_1 excited states and their character (right). The corresponding NTOs are reported in Figure S24.

Table 1. Adiabatic Labels (State) and Adiabatic ^{3}MLCT and ^{3}ILCT Energies (ΔE_{adia}) for $[Ru(4,4'\text{-btfmb})_3]^{2+}$, Ru-phen, and Ru-*n*T ($n$ = 0−4) in a Water Environment at the TD-M06/6-31+G/SDD Level of Theory**[a]

	^{3}MLCT		^{3}ILCT	
compound	state	ΔE_{adia} (eV)	state	ΔE_{adia} (eV)
$[Ru(4,4'\text{-btfmb})_3]^{2+}$	T_1	2.01		
Ru-phen	T_1	1.91		
Ru-0T	T_1	1.91		
Ru-1T	T_1	1.91		
Ru-2T	T_1	1.91		
Ru-3T	T_2	1.99	T_1	1.54
Ru-4T	T_2	1.88	T_1	1.42

[a]Additional details can be found in Table S5.

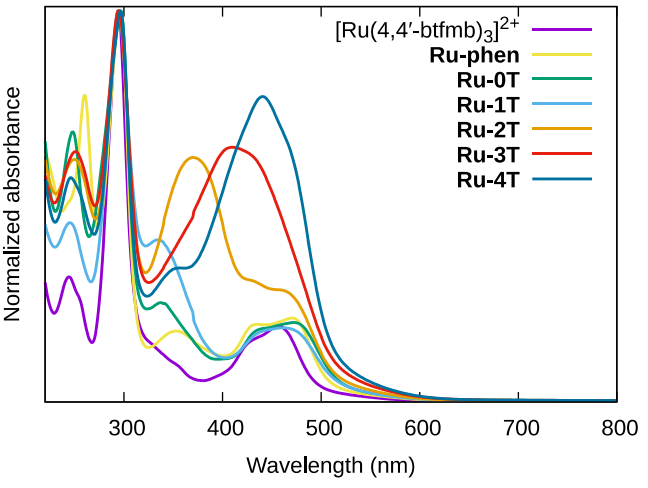

Figure 7. UV−vis spectra of $[Ru(4,4'\text{-btfmb})_3]^{2+}$, **Ru-phen**, and **Ru-*n*T** (n = 0−4) normalized to the π−π^* peak near 295 nm.

character and length of the nT chain as we have seen previously.[17,51]

3.3. Spectroscopy. *3.3.1. Electronic Absorption.* The UV−vis absorption spectra of the series are overlaid in Figure 7, and the corresponding molar extinction coefficients for various peak maxima are summarized in Table 2. The spectra display some of the general features of typical Ru(II) polypyridyl complexes[81] but with some distinctions for the complexes bearing IP-*n*T ligands. The sharp peaks near 295 nm and shorter are due to π−π^* transitions involving the 4,4′-btfmb ligand,[55] as well as phen and/or IP in the cases of **Ru-phen** and **Ru-*n*T**. The energies of these transitions are not affected by the length of the thiophene chain appended to the IP ligand. The broader and less intense peaks between 400 and 500 nm with a local maximum at 456 nm in $[Ru(4,4'\text{-btfmb})_3]^{+2}$ are due to $Ru^{2+}(d\pi) \rightarrow L(\pi^*)$ ^{1}MLCT transitions involving mainly the 4,4′-btfmb ligands as the π^* acceptor orbitals. The substitution of one 4,4′-btfmb ligand for phen or IP causes the lowest-energy ^{1}MLCT transitions to red shift by 10−20 nm. Assuming that the 4,4′-btfmb π^* orbitals remain the acceptor orbitals for the lowest-energy ^{1}MLCT transitions in all cases, the effect of phen or IP is primarily on the $d\pi$ orbital energy. This effect is most evident for **Ru-phen**, **Ru-0T**, and **Ru-1T**. For complexes containing the IP-*n*T ligand, additional transitions overlap the ^{1}MLCT transitions. These contributions from the IP-*n*T ligands can be seen in the absorption spectra of the analogous uncomplexed IP-*n*T ligands and free oligothiophenes.[82] The computed NTOs provide information on their contributions and characters in the Ru(II) complexes (Figures 5 and S23). The lowest-energy singlet−singlet transition is mixed ^{1}MLCT/^{1}LLCT for **Ru-2T**

https://doi.org/10.1021/acs.inorgchem.3c04382
Inorg. Chem. XXXX, XXX, XXX−XXX

Table 2. Molar Extinction Coefficients at Selected Wavelengths for the Complexes of This Study

cmpd	λ_{abs} (nm) (log (ε/M^{-1} cm^{-1}))
$[Ru(4,4'\text{-btfmb})_3]^{+2}$	244 (4.34), 294 (4.84), 427 (4.01), 456 (4.12)
Ru-phen	260 (4.69), 296 (4.80), 353 (4.05), 432 (4.09), 471 (4.12)
Ru-0T	248 (4.68), 296 (4.84), 341 (4.13), 435 (4.12), 470 (4.13)
Ru-1T	245 (4.57), 294 (4.92), 335 (4.51), 462 (4.20)
Ru-2T	250 (4.68), 295 (4.89), 370 (4.69), 462 (4.35)
Ru-3T	251 (4.58), 294 (4.76), 410 (4.57), 426 (4.55)[a]
Ru-4T	246 (4.57), 297 (4.81), 351 (4.33), 441 (4.70), 468 (4.62)[a]

[a]The maximum of the longest wavelength singlet−singlet transition is obscured.

wherein ^{1}LLCT involves nT → 4,4′-btfmb CT, while these transitions are mixed ^{1}LLCT/^{1}IL/^{1}ILCT and ^{1}LLCT/^{1}ILCT/^{1}IL for **Ru-3T** and **Ru-4T**, respectively. In these cases, ^{1}LLCT is the major contributor and involves nT → IP CT, ^{1}ILCT involves nT → nT CT, and ^{1}IL involves localized $\pi\pi^*$ transitions within nT. These mixed transitions shift to longer wavelengths and increase in ^{1}ILCT character with increasing n as we have observed previously in related compounds.[11,17,46,47,51]

3.3.2. Singlet Oxygen Sensitization. The singlet oxygen quantum yields (Φ_Δ) of the complexes were calculated by measuring the intensity of O_2 phosphorescence ($^1\Delta_g \rightarrow {}^3\sum_g$) centered at 1260 nm against $[Ru(bpy)_3]^{2+}$ as the standard (Φ_Δ = 0.56).[83] These are reported in Table 3. $[Ru(4,4'\text{-btfmb})_3]^{2+}$, **Ru-phen**, and **Ru-0T** are moderately efficient $^1O_2$ generators (Φ_Δ = 0.47−0.64) and similar to $[Ru(bpy)_3]^{2+}$. However, the thiophene-containing complexes **Ru-1T**−**Ru-4T** exhibit larger differences (Φ_Δ = 0.13−0.66) and are less efficient than what has been observed for related compounds.[11,47] The largest $^1O_2$ quantum yield was measured for **Ru-3T** at 66%. While all of the complexes show a wavelength-dependence for Φ_Δ, **Ru-4T** exhibits a notable concentration dependence for the $^1O_2$ quantum yield (Figure S25 and Table S6). These differences in Φ_Δ appear to be unrelated to differences in other photophysical parameters such as emission wavelengths and triplet lifetimes (vide infra).

3.3.3. Emission. All of the complexes in the series exhibited a broad, featureless red emission band at room temperature (Figure 8a and Table 3). This emission was centered around 636 nm (τ_{em} = 1.5 μs) for the parent $[Ru(4,4'\text{-btfmb})_3]^{2+}$ complex in MeCN at room temperature (RT) and shifted to shorter wavelengths with vibronic intervals of around 1350 cm^{-1} at 77 K (Figure 4b).[54−57] Such behavior is consistent with emissive ^{3}MLCT states in Ru(II) complexes with polypyridyl ligands.[84] The thermally induced Stokes shift (ΔE_S) of around 830 cm^{-1} is slightly smaller than the related model complex $[Ru(bpy)_3]^{2+}$ (ΔE_S = 1127 cm^{-1})[85] but in agreement with the assignment.[86] Similar to what was observed for the ^{1}MLCT absorption bands, the introduction of a phen or an IP ligand results in bathochromic shifts of up to 30 nm but otherwise similar spectra and lifetimes (τ_{em} = 0.8−0.9 μs). The ^{3}MLCT emission energies and lifetimes (τ_{em} = 0.6−0.8 μs) also do not depend on the number of thiophenes in the IP-nT ligand, suggesting that the π^* acceptor orbitals in the Ru(dπ) → L(π^*) transitions involve the 4,4′-btfmb coligands. The emission quantum yield (Φ_{em}) ranges from 16% for $[Ru(4,4'\text{-btfmb})_3]^{2+}$ to 9% for the complexes without thienyl groups. The value of Φ_{em} drops to around 2% for **Ru-1T**, and additional thienyl rings further decrease the emission output to <1%. Although **Ru-4T** produces weak but detectable emission, a value for Φ_{em} was not calculated due to the extremely low signal-to-noise ratio. The values for Φ_{em} increase up to 10-fold at 77 K but **Ru-4T** is still only about 0.14%. While the energy of the emissive ^{3}MLCT state does not appear to change across the series, the emission quantum yields decrease with increasing n and implicate additional excited-state deactivation pathways. The computed NTOs indicate that the nature of T_1 changes substantially with the introduction of three or four thienyl groups. The lowest-energy triplet states are of ^{3}MLCT character for all of the complexes except **Ru-3T** and **Ru-4T**, where T_1 becomes mixed ^{3}ILCT/^{3}LLCT/^{3}IL (with ^{3}ILCT involving nT → nT CT, ^{3}LLCT involving nT → IP CT, and ^{1}IL based on localized $\pi\pi^*$ transitions within n). These organic triplets involving the IP-nT ligand are nonemissive, and thus the very weak emission arises from the ^{3}MLCT state that is T_2 for **Ru-3T** and **Ru-4T** and of similar energy to the other complexes in the series.

3.3.4. Transient Absorption and Excited-State Pathways. The triplet excited states were investigated using nanosecond transient absorption (TA) spectroscopy with excitation from a 355 nm (Figure 9) or 532 nm laser (Figure S26) of ≲5 ns pulse width. The responses with the two different excitation wavelengths are similar, suggesting similar excited-state dynamics. The differential excited-state absorption (ESA) spectra were collected using solutions of PF_6^- salts of the compounds in degassed (5× freeze−pump−thaw) MeCN. Early time slices are presented in Figures 9 and S26, and the full set of relaxation spectra over different time points are collected in Figures S27 and S28. Transient lifetimes were measured at the ESA maxima and bleach minima and are listed in Table 3.

Table 3. Spectroscopic Data for Compounds $[Ru(4,4'\text{-btfmb})_3](PF_6)_2$, Ru-phen, and Ru-0T−Ru-4T as PF_6^- Salts[a]

	RT emission			77 K emission			τ_{TA}/μs	
cmpd	λ_{em} (λ_{ex})/nm	Φ_{em}	τ_{em}/μs	λ_{em} (λ_{ex})/nm	$\Phi_{em,77K}$	Φ_Δ (λ_{ex}/nm)	λ_{ex} = 355 nm	λ_{ex} = 532 nm
$[Ru(4,4'\text{-btfmb})_3]^{2+}$	636 (458)	1.6×10^{-1}	1.5	604, 653 (460)	2.5×10^{-1}	0.47 (462)	1.5	1.5
Ru-phen	660 (470)	9.0×10^{-2}	0.89	619, 668 (472)	2.4×10^{-1}	0.64 (470)	0.89−0.94	0.77−0.92
Ru-0T	662 (470)	9.1×10^{-2}	0.83	619, 669 (470)	1.9×10^{-1}	0.50 (469)	0.78−0.86	0.78−0.87
Ru-1T	661 (460)	1.8×10^{-2}	0.79	620, 670 (469)	2.0×10^{-1}	0.13 (462)	0.81−0.93	0.71−0.87
Ru-2T	659 (457)	4.1×10^{-3}	0.62	634, 687 (463)	4.3×10^{-2}	0.28 (466)	0.61−0.72	0.63−0.71
Ru-3T	664 (462)	1.3×10^{-3}	0.79	623, 673 (470)	9.7×10^{-3}	0.66 (470)	20−21	22−24
Ru-4T	650 (435)	v. wk.	0.64	625, 672 (468)	1.4×10^{-3}	0.40 (467)	19−20	20−21

[a]Excitation wavelengths are indicated in parentheses. Emission lifetimes were measured following a <5 ns 355 nm laser pulse.

https://doi.org/10.1021/acs.inorgchem.3c04382
Inorg. Chem. XXXX, XXX, XXX−XXX

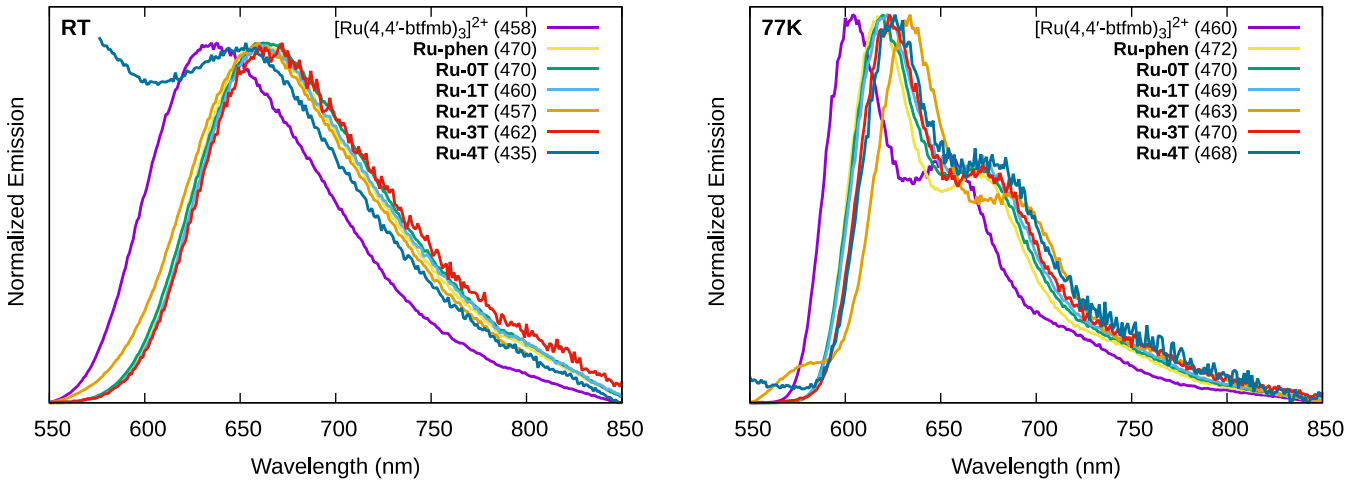

Figure 8. Normalized emission spectra $[Ru(4,4'\text{-btfmb})_3]^{2+}$ and the **Ru-*n*T** series as PF_6^- salts at RT and 77 K. The RT emission was measured in MeCN degassed by freeze−pump−thaw (five cycles). The 77 K emission was measured in a 4:1 EtOH/MeOH glass. Excitation wavelengths are noted in parentheses.

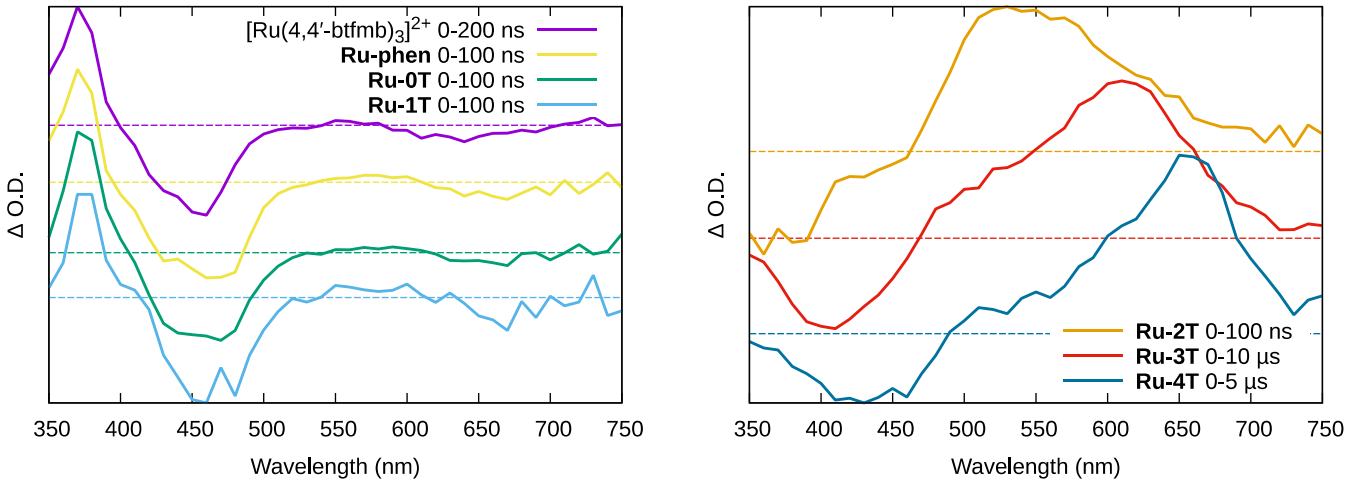

Figure 9. Transient absorption (TA) spectra of $[Ru(4,4'\text{-btfmb})_3](PF_6)_2$, **Ru-phen**, and **Ru-*n*T** as PF_6^- salts in degassed MeCN at RT (λ_{ex} = 355 nm) integrated over the indicated time slice following the excitation pulse. The profiles for λ_{ex} = 532 nm are similar (Figure S26). The horizontal dashed lines indicate ΔO.D. = 0 for each compound differentiated by color.

The ESA profiles of $[Ru(4,4'\text{-btfmb})_3]^{2+}$, **Ru-phen**, **Ru-0T**, and **Ru-1T** are similar, consisting primarily of a strong ^{1}MLCT ground-state bleach near 450 nm superimposed with new ESA characteristic of the ^{3}MLCT state. The stronger ESA near 375 nm involves 4,4′-btfmb$^-$ transitions, and the extremely weak and broad absorption past 525 nm is due to 4,4′-btfmb$^-$ or LMCT transitions involving Ru(II). The TA lifetimes match the emission lifetimes and support lowest-lying ^{3}MLCT states for these complexes as predicted from the NTO analyses.

The ESA profile of **Ru-2T** exhibits features consistent with a triplet excited-state localized to the IP-*n*T ligand, as we have previously reported.[11,17,50,51,87−89] This broad and rather intense ESA near 450−700 nm is superimposed on the bleach with its minimum near 370 nm due to a strong ground-state absorption contributed by the IP-2T ligand (Figure 9). While **Ru-2T** has the signature of an *n*T-based triplet, its TA lifetime matches the emissive ^{3}MLCT lifetime at all wavelengths. This observation and the NTO analyses suggest that the ^{3}MLCT state computed as T_1 and the ligand-localized triplet are close in energy and decay with a common lifetime.[90] In this regard, **Ru-2T** behaves differently from some its close analogues containing the IP-2T ligand, where T_1 is of mixed ^{3}LLCT/^{3}ILCT character with a prolonged lifetime,[51] due to the lower ^{3}MLCT energies of Ru(II) polypyridyl complexes incorporating 4,4′-bftmb coligands.

The ESA spectra of **Ru-3T** and **Ru-4T** are characteristic of oligothiophene-based ^{3}ILCT states, with longer TA lifetimes. The excited-state relaxation pathways are proposed in Scheme 1. **Ru-3T** shows a bleach corresponding to the ground-state $\pi\pi^*$ transition near 410 nm and a broad ESA with its maximum near 610 nm. For **Ru-4T**, these were shifted to around 430 and 655 nm, respectively. These ESA features are similar to those of the free IP-3T and IP-4T ligands.[46,49] The decays are monoexponential, with τ = ∼20 μs for both complexes, indicating that the long-lived ^{3}ILCT is decoupled from the shorter-lived emissive ^{3}MLCT with computed T_2 energies near 1.9−2.0 eV. This is further supported by the very low emission quantum yields for **Ru-3T** and **Ru-4T** and computed T_1 energies of 1.54 and 1.42 eV, respectively, with significant ^{3}ILCT character.

3.4. Electrochemistry. The electrochemistry of Ru(II) polypyridyl complexes is typified by single electron processes

https://doi.org/10.1021/acs.inorgchem.3c04382
Inorg. Chem. XXXX, XXX, XXX−XXX

Scheme 1. Jablonski Diagram Illustrating the Excited-State Relaxation Pathways of Complexes Ru-3T and Ru-4T; Energies are not to scale

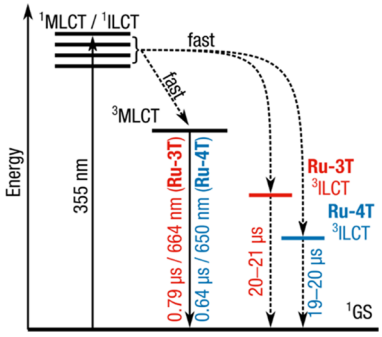

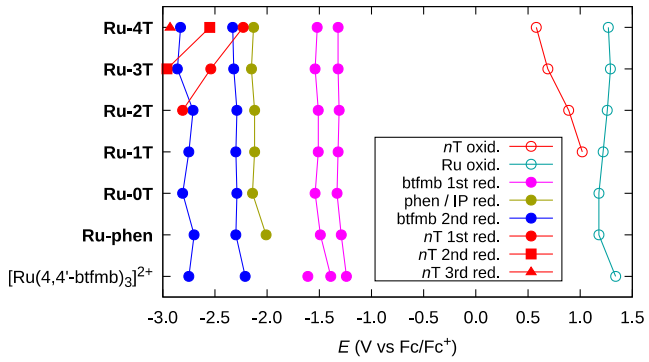

Figure 10. Redox potentials (vs Fc) of $[Ru(4,4'\text{-btfmb})_3]^{2+}$, **Ru-phen**, and **Ru-*n*T** as PF_6^- salts in degassed MeCN at RT and their tentative assignments.

involving one-electron oxidation of the metal center and three sequential reductions on each of the ligands.[91] Oxidation of the Ru^{2+} center (+0.98 V versus Fc, MeCN) tends to be electrochemically reversible, and the ensuing low-spin $4d^5$ complex is chemically stable. In complexes like $[Ru(bpy)_3]^{2+}$, the first reduction (−1.72 V versus Fc, MeCN) involves the lowest-energy ligand π^* orbital. Since the low-spin $4d^6$ configuration is thereby unaffected, the complex remains substitutionally inert, and the process is also reversible. The added electron is localized on one ligand, and thus $[Ru(bpy)_3]^{2+}$ exhibits three sequential one-electron reductions under straightforward electrochemical conditions. In a potential window widened by low temperature cyclic voltammetry, $[Ru(bpy)_3]^{2+}$ has been shown to participate in a total of six one-electron reductions.[92,93]

There are additional redox processes for some members of the present series due to the presence of the electrochemically active oligothiophene[94] unit in complexes **Ru-2T**−**Ru-4T**. The formal redox potentials of the series were measured by cyclic differential pulse voltammetry (CDPV) to enhance the signal, with ferrocene (Fc) as an internal reference ($E_{1/2}$ (Fc/Fc$^+$) = 0.380 V vs SCE[95]). The potentials are compiled in Table 4 and compared graphically in Figure 10 with tentative assignments. The CDPV plots for oxidation and reduction are shown in Figures S29 and S30, respectively.

The metal oxidation of $[Ru(4,4'\text{-btfmb})_3]^{2+}$ and the three one-electron reductions agree well with published data[55] and are around 0.3−0.5 V more positive than the corresponding processes in $[Ru(bpy)_3]^{2+}$, a consequence of the electron-withdrawing nature of the 4,4′-btfmb ligands. The shift of the $Ru^{2+}\rightarrow Ru^{3+}$ oxidation is slightly attenuated when one 4,4′-btfmb ligand is replaced with phen or IP-*n*T. The oxidation of *n*T becomes more favorable with increasing *n*, consistent with the behavior of free oligothiophenes.[96] The oxidation potential of the thienyl group ranges from +1.02 V for **Ru-1T** to +0.58 for **Ru-4T** and is less positive than the metal center in all cases, indicating that *n*T is more easily oxidized than Ru(II) regardless of the number of thiophenes. The oxidation of *n*T does shift the $Ru^{2+}\rightarrow Ru^{3+}$ oxidation slightly more positive, consistent with a decrease in electron density on the metal. For **Ru-3T** and **Ru-4T** there is at least one additional peak between those for *n*T and Ru^{2+} oxidation that is of lesser intensity and solvent-dependent (Figure S29). This peak, not listed in Table 4, is thought to arise from the oxidation of the σ-dimer radical cation ($(Ru\text{-}nT)_2^{+\bullet} \rightarrow (Ru\text{-}nT)_2 + 2H^+ + e^-$) given the known abilities of certain oligothiophenes to undergo electrochemical σ-dimerization through their α positions. However, this requires further investigation to confirm.

$[Ru(4,4'\text{-btfmb})_3]^{2+}$ and the other complexes without thiophenes (**Ru-phen**, **Ru-0T**) as well as **Ru-1T** exhibit five sequential reductions spanning −1.24 to −2.81 V (Figure 10). For $[Ru(4,4'\text{-btfmb})_3]^{2+}$, this involves sequential one-electron reductions on each of the three 4,4′-btfmb ligands followed by second reductions on two of those ligands (within the experimental potential window). We believe this study is the first to report the second reductions of the two 4,4′-btfmb ligands occurring between −2.2 and −2.9 V for $[Ru(4,4'\text{-btfmb})_3]^{2+}$.

When one of the 4,4′-btfmb ligands is replaced by phen, IP-0T, or IP-1T, the third reduction involves phen or IP and is less favorable by around 0.4−0.5 V (owing to their lack of electron-withdrawing $-CF_3$ substituents). **Ru-2T**−**Ru-4T** exhibit similar reductions involving the 4,4′-btfmb coligands and IP, but they accommodate additional reductions on the

Table 4. Formal Redox Potentials for the Hexafluorophosphate Salts of the Complexes Measured Using CDPV at Approximately 1.0 mM in MeCN Containing TBAPF$_6$[a]

compound	$nT^{2-}\rightarrow nT^{3-}$	$nT^{-}\rightarrow nT^{2-}$	$nT\rightarrow nT^{-}$	$LL_2^{-}\rightarrow LL_2^{2-}$	$LL_1^{-}\rightarrow LL_1^{2-}$	$LL_3\rightarrow LL_3^{-}$	$LL_2\rightarrow LL_2^{-}$	$LL_1\rightarrow LL_1^{-}$	$Ru^{2+}\rightarrow Ru^{3+}$	$nT\rightarrow nT^{+}$
$[Ru(4,4'\text{-btfmb})_3]^{2+}$				−2.75	−2.21	−1.61	−1.39	−1.24	+1.34	
Ru-phen				−2.70	−2.30	−2.01	−1.49	−1.29	+1.18	
Ru-0T				−2.81	−2.29	−2.14	−1.54	−1.33	+1.18	
Ru-1T				−2.75	−2.30	−2.12	−1.51	−1.32	+1.22	+1.02
Ru-2T			−2.81	−2.71	−2.29	−2.12	−1.51	−1.31	+1.26	+0.89
Ru-3T		−2.96	−2.54	−2.86	−2.32	−2.15	−1.54	−1.32	+1.29	+0.69
Ru-4T	−2.93	−2.55	−2.23	−2.83	−2.33	−2.13	−1.52	−1.32	+1.27	+0.58

[a]The potentials are referenced in volts (V) against ferrocene as the internal standard. The working and reference electrodes were glassy carbon and Ag/AgCl/4 M KCl, respectively. Overlapping waves were deconvoluted mathematically (error approximately ±0.02 V).

https://doi.org/10.1021/acs.inorgchem.3c04382
Inorg. Chem. XXXX, XXX, XXX−XXX

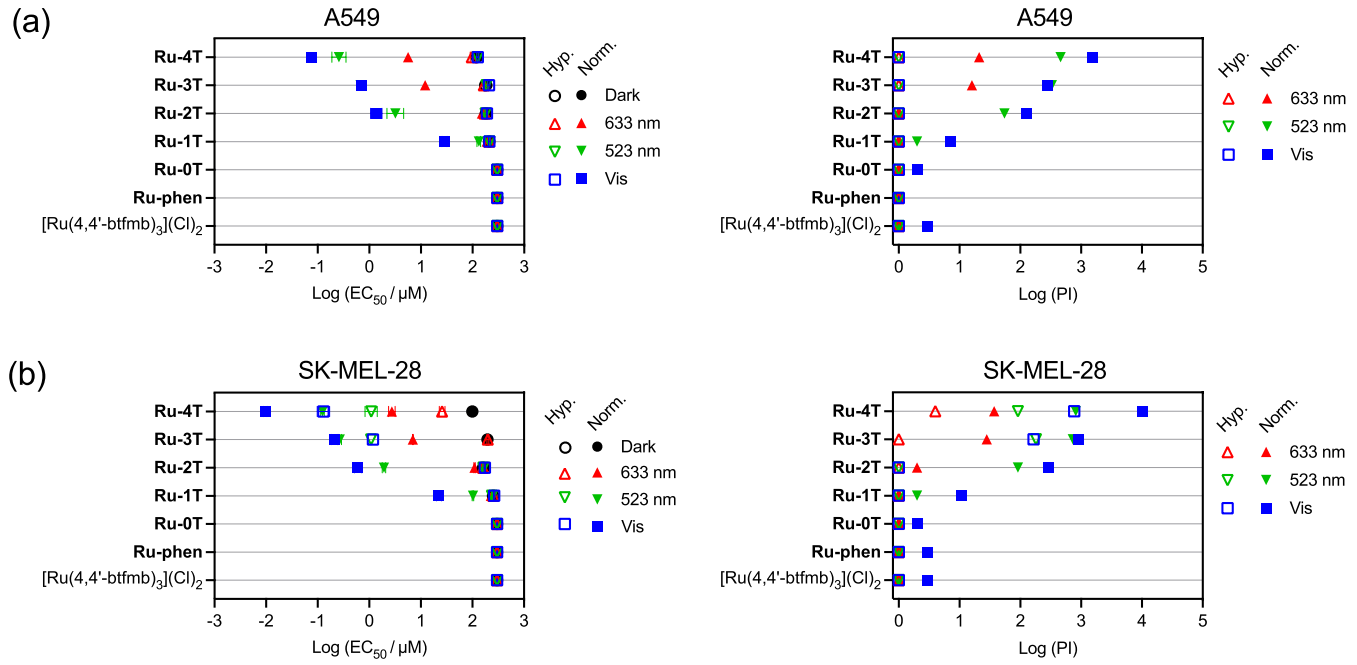

Figure 11. In vitro cytotoxicity and photocytotoxicity log (EC_{50} ± SEM) values (left) and PI values (right) obtained from dose−response curves in the SK-MEL-28 melanoma cell line (a) and A549 cell line (b) with $[Ru(4,4'\text{-btfmb})_3](Cl)_2$ and **Ru-phen**−**Ru-4T**. Treatments include dark (black circles) or light delivered at a fluence of 100 J cm^{-2} and irradiance of ∼20 mW cm^{-2}. The light wavelengths were broadband-visible (400−700 nm, blue squares), 523 nm (green inverted triangles), or 633 nm (red triangles). Data collected under normoxic (∼18.5% O_2) and hypoxic (1% O_2) conditions is represented with closed symbols and open symbols, respectively.

oligothienyl groups. For **Ru-2T**, the 2T group accepts only one electron and this sixth reduction is the least favorable and occurs near −2.81 V. The 3T group of **Ru-3T** can be doubly reduced (−2.54 and −2.96 V), where the first *n*T reduction is easier than the last 4,4′-btfmb reduction. Continuing this trend, the 4T group of **Ru-4T** accommodates three electrons (−2.23, −2.55, and −2.93 V), with the first *n*T reduction occurring near that of IP at −2.13 V. The effect of the thiophene chain length is dramatic. The *n*T reduction potential shifts positive by more than 0.5 V on going from two to four thiophenes, and the **Ru-4T** complex can accommodate at least eight extra electrons in its ground state at room temperature.

3.5. In Vitro Photobiological Activity. The compounds in this series were assessed for their cytotoxicity in the absence of light (dark) as well as their light-triggered cytotoxicity against human skin melanoma cells (SK-MEL-28) and lung carcinoma cells (A549) cultured as 2D monolayers (Figure 11). The experimental details can be found in our previously published work[11,17,20] as well as in the SI. The spectral output of the light sources is shown in Figure S31, their overlap with the absorption profiles of the complexes is shown in Figure S32, and the estimated absorbed photon flux is compiled in Table S7. The results are summarized in Figure 11 and Tables S8, S9.

3.5.1. Normoxia. For each photobiological assay in normoxia, SK-MEL-28 or A549 cells were seeded into two sets of 384-well plates: one for dark cytotoxicity evaluation and the other for photocytotoxicity assessment. After allowing the cells to adhere for 3−5 h at 37 °C, cells were dosed with the compounds (1 nM to 300 μM). The light plates were exposed to light treatments after a 13−22 h DLI, while the dark plates remained in the incubator. The light treatments were delivered at a fluence of 100 J cm^{-2} emitted from broadband-visible (400−700 nm, 21 mW cm^{-2}) or monochromatic (±2.5 nm) green (523 nm, 18 mW cm^{-2}) or red (633 nm, 18 mW cm^{-2}) LEDs.

After light treatment, the plates were allowed to incubate in normoxia at 37 °C for 24 h. Cell viability was then assessed indirectly using a resazurin-based cell viability assay. Sigmoidal fits of the dose−response curves were used to calculate the effective concentrations required to reduce cell viability by 50% (EC_{50} values) for both treatment conditions. The amplified cytotoxic effects upon light exposure, known as photo-therapeutic indices (PIs), were calculated as ratios of dark EC_{50} to light EC_{50} values.

The complexes were mostly nontoxic to both cell lines in the dark. $[Ru(4,4'\text{-btfmb})_3]^{2+}$, **Ru-phen**, and **Ru-0T** exhibited dark EC_{50} values that exceeded the highest doses used in the assay (>300 μM), indicating a lack of toxicity. They were also inactive against both cell lines under any light condition. **Ru-1T**−**Ru-3T** were considered nontoxic toward both cell lines, with dark EC_{50} values >170 μM. **Ru-4T** had the lowest dark EC_{50} values, which were still relatively high at 100 and 120 μM in SK-MEL-28 and A549 cells, respectively.

3.5.1.1. SK-MEL-28 Cells. Increasing the number of thiophene rings (*n* = 1−4 thienyl groups) increased the potency with visible light, ranging from 22 μM (PI = 11) for **Ru-1T** to as low as 10 nM (PI = 10,000) for the most potent compound **Ru-4T** in SK-MEL-28. Appending two thiophenes (**Ru-2T**) improved the potency 36-fold, shifting the EC_{50} values to submicromolar values near 0.61 μM (PI = 290). About 100-fold enhancement in photocytotoxicity was seen moving to three thiophene rings (**Ru-3T**; SK-MEL-28: EC_{50} = 0.21 μM, PI = 920), and over 2000-fold improvement occurred with four thiophenes (**Ru-4T**; SK-MEL-28: EC_{50} = 10 nM, PI = 10,000).

The activity of the series was mostly diminished with longer-wavelength green or red light. With green light, **Ru-1T** lost

https://doi.org/10.1021/acs.inorgchem.3c04382
Inorg. Chem. XXXX, XXX, XXX−XXX

most of its activity (EC_{50} = 103 μM, PI = 2). The activity of **Ru-2T** dropped by a factor of 3 but was still single-digit micromolar (EC_{50} = 1.9 μM, PI = 91), and that of **Ru-4T** dropped by 10-fold but remained submicromolar (EC_{50} = 0.12 μM, PI = 815). **Ru-3T**, on the other hand, maintained its activity (EC_{50} = 0.27 μM, PI = 731). With red light, **Ru-3T** (EC_{50} = 7.02 μM; PI = 731) and **Ru-4T** (EC_{50} = 2.74 μM; PI = 815) showed modest activity. This outcome aligns with the anticipated behavior of compounds that exhibit minimal absorption of red light.[97]

3.5.1.2. A549 Cells. The A549 cell line proved more resistant to the light-triggered compounds than SK-MEL-28 under similar conditions, but the overall trend in activity remained the same. **Ru-1T** (visible EC_{50} = 29 μM, PI = 7) was the least active thienyl complex, followed by **Ru-2T** (visible EC_{50} = 1.37 μM, PI = 127), **Ru-3T** (visible EC_{50} = 0.70 μM, PI = 280), and finally **Ru-4T** (EC_{50} = 0.077 μM, PI = 1500). Treatments with red and green light similarly attenuated the overall activity of the series.

3.5.2. Hypoxia. The assays under hypoxic conditions mirrored the procedure followed for normoxia, with a notable exception: after cell adhesion, the plates—both for dark and light conditions—were transferred to a hypoxia chamber with 1% O_2 atmosphere for a duration of 2−3 h prior to introducing the compounds. After a DLI of 18 h in the hypoxia chamber, the concentration of dissolved O_2 was verified in the assay wells using an immersive optical probe before sealing the plates to be light-treated with a transparent qPCR film that has a low gas permeability. Light was delivered outside the hypoxia chamber for approximately 1.5 h, while the dark plates were kept inside an incubator. The films were removed from the light plates at the end of the illumination period. Both dark and light plates were then incubated in normoxia (37 °C, 5% CO_2, with relative humidity above 90%) for 20−23 h, after which time the cell viability was assessed.

Hypoxic conditions broadly attenuated the activity of the series in both cell lines, where A549 cells were completely resistant to all treatments and SK-MEL-28 cells were moderately sensitive under certain conditions. Regardless of light treatment, $[Ru(4,4'\text{-btfmb})_3](Cl)_2$ and compounds **Ru-0T**−**Ru-2T** exhibited no photocytotoxic effect under hypoxic conditions toward SK-MEL-28 cells. On the other hand, **Ru-3T** showed an EC_{50} value of ∼1 μM with visible and green light treatments. With red light, **Ru-4T** was less active (EC_{50} = 26 μM, PI = 4), but otherwise the series was inactive. The dramatic decline in the activity of **Ru-3T** and **Ru-4T**, coupled with the complete inactivity of the other compounds in the series under hypoxic conditions, suggests that oxygen plays a pivotal role in their photocytotoxic mechanisms. This observation solidifies the hypothesis that the primary driver behind the observed photocytotoxicity of these compounds in normoxic conditions stems from oxygen-dependent photophysical processes.

3.5.3. Biological Replicates. Figure 11 and Table S9 show representative activity against SK-MEL-28 for one biological replicate based on the mean values from three technical replicates with minimal standard deviation. Since a greater degree of variation is expected over biological replicates, we assessed the activity of the compounds (**Ru-3T** and **Ru-4T**) of highest activity over five biological replicates (each carried out in triplicate) with SK-MEL-28 cells, as illustrated in Figure S34 and detailed in Tables S10−S13. Repeat 0 corresponds to the data in Figure 11 and Table S9. The subsequent biological replicates are labeled Repeats 1−5. SK-MEL-28 cells were selected for these studies because this is the cell line we have historically used to rank potency across all compounds made in our laboratory.[17]

Ru-3T and **Ru-4T** were nontoxic over all biological replicates in both normoxia and hypoxia without light activation, with mean EC_{50} values of 197 μM for **Ru-3T** and 100 μM for **Ru-4T**. The visible EC_{50} values for **Ru-3T** in normoxia were in the range of 70−700 nM (mean = 440 nM), and their visible PIs spanned 305−2700 (PI_{avg} = 1400). The EC_{50} values for **Ru-4T** under the same conditions ranged from 9 to 59 nM with a mean of 17 nM (PI = 1900−12,000, mean = 6500). The results from all six replicates varied less than an order of magnitude.

Using green light in normoxia, the EC_{50} values for **Ru-3T** fluctuated between 0.22 and 0.66 μM , with PIs between 300 and 1000. The mean values were determined to be 0.44 μM and 548, respectively. For **Ru-4T**, the results were slightly more variable, with green EC_{50} values ranging from 54 to 320 nM, and the corresponding PIs falling in the 800 to 2000 range. Even though **Ru-4T** was generally more active than **Ru-3T**, the difference in their activities was only around 3-fold.

Under red light illumination in normoxia, the EC_{50} values for **Ru-3T** and **Ru-4T** were reproducibly in the single-digit micromolar regime. **Ru-3T** exhibited red EC_{50} values between 2 and 7 μM (mean = 4.6 μM) and PIs ranging from 23 to 101 (PI_{avg} = 52). The activity of **Ru-4T** was slightly more consistent than **Ru-3T**, with red EC_{50} values falling between 1.3 and 3.3 μM (mean = 2.2 μM) with PIs between 21 and 91 (PI_{avg} = 53). The responses with red light for **Ru-3T** and **Ru-4T** are notable as both complexes exhibit vanishingly low molar extinction coefficients at 633 nm. This characteristic has been reported previously,[97] and tends to require lowest-lying $^3\pi\pi^*$ triplets with prolonged lifetimes such as those observed for **Ru-3T** and **Ru-4T**.

The activity of **Ru-3T** in hypoxia was mostly consistent but repeats 3 (with red light) and 4 (with vis and green) were outliers: repeat 3 displayed unusually high red activity compared to the other replicates, and no activity at all was observed in repeat 4. In some of the replicates, the visible and green activity of **Ru-3T** improved when compared to our initial measurements, but all values were still within an order of magnitude. With visible light, the EC_{50} value was 1.2 μM (PI = 170) in repeat 0 but improved to a range of 300−870 nM (PI = 230−700, PI_{avg} = 300). Similarly, the initial green EC_{50} value for **Ru-3T** was 1.1 μM (PI = 180), which lowered to 0.3−1.0 μM (PI = 200−700, PI_{avg} = 270) in subsequent assays. The observation of two distinct outliers, and the fact that the activity of **Ru-3T** was actually greater in subsequent biological replicates, underscores the importance of performing biological replicates when evaluating photobiological efficacy.

The activity of **Ru-4T** varied slightly more in hypoxia than it did in normoxia, but all EC_{50} values were still within roughly 1 order of magnitude. Using visible light treatment, repeats 0 and 2−5 fell between 0.13 and 0.54 μM (PI = 200−400), but repeat 1 presented a slightly lower EC_{50} of 35 nM (PI = 2900). With green and red light treatments, **Ru-4T** proved to be consistently more active than what was originally observed in repeat 0, with initial EC_{50} values of 1.0 μM (PI = 90) and 26 μM (PI = 4), respectively, which improved to a range of 200−900 nM (PI = 100−500, PI_{avg} = 210) and 3−9 μM (PI = 7−30, PI_{avg} = 21) during replicates 1−5. The average hypoxic red EC_{50} (<10 μM) of **Ru-4T** is particularly notable for this class

https://doi.org/10.1021/acs.inorgchem.3c04382
Inorg. Chem. XXXX, XXX, XXX−XXX

of PS and is comparable to the "ubertoxin" ML19C01 (which presents subnanomolar normoxic phototoxicity).[17,20]

In conclusion, across six biological replicates, **Ru-4T** has consistently displayed superior activity compared to **Ru-3T**, particularly when activated with visible light under normoxic conditions. Under these conditions, **Ru-4T** had an average EC_{50} of 24 nM (PI_{avg} = 6500). Notably, the values obtained in all biological replicates were within an order of magnitude, making **Ru-4T** more consistent than ML19C01, which varies by up to 6 orders of magnitude.[17,20] This marked improvement in consistency may be related to the improved aqueous solubility observed in this family of complexes, and the effect of fluorination on biological reproducibility is being investigated further.

4. CONCLUSIONS

Herein, we synthesized a family of Ru(II) polypyridyl complexes featuring two 4,4′-btfmb coligands and the IP-*n*T ligand (n = 1−4) and compared these systems to the reference compounds $[Ru(4,4'\text{-btfmb})_3]^{2+}$, **Ru-phen**, and **Ru-0T**. This study stands as part of our larger initiative to examine the impact of structural variations on the physicochemical, photophysical, electrochemical, and (photo)biological properties of oligothienyl-containing metal complexes.

The complexes lacking thienyl groups and **Ru-1T** are relatively hydrophilic, while the lipophilicities of **Ru-2T**−**Ru-4T** increase with n. The number of thienyl groups in the **Ru-*n*T** complexes also have a striking influence on the ground-state absorption and TA spectra with transitions involving the *n*T groups (^{1}LLCT and ^{1}ILCT) shifting to longer wavelengths and increasing in ^{1}ILCT character with increasing n. Based on their TA profiles, **Ru-3T** and **Ru-4T** have lowest-lying ^{3}ILCT states, while the complexes lacking *n*T groups and **Ru-1T** as well as **Ru-2T** have ^{3}MLCT states as T_1. The TA lifetimes corroborate this assignment with **Ru-3T** and **Ru-4T** having triplet lifetimes on the order of 20−24 μs and ESA spectra consistent with ^{3}ILCT states. The other complexes have triplet lifetimes and TA spectra consistent with ^{3}MLCT states near 1 μs. The exception is **Ru-2T**, which has the signature of an *n*T-localized triplet but with a lifetime characteristic of the ^{3}MLCT state. All of the complexes have emissive ^{3}MLCT states, but with emission quantum yields that decrease with increasing n. The $^1O_2$ quantum yields increase from 13 to 66% from one to three thiophenes but decrease to 40% at four. The parent complexes lacking thienyl groups generate $^1O_2$ better than the **Ru-*n*T** complexes, with the exception that **Ru-3T** is slightly more efficient than **Ru-phen**.

Compared to Ru(II) polypyridyl complexes such as $[Ru(bpy)_3]^{2+}$, the parent $[Ru(4,4'\text{-btfmb})_3]^{2+}$ complex is oxidized less readily but is reduced more easily owing to the electron-withdrawing nature of the $-CF_3$-substituted bipyridyl coligands. All of the complexes undergo at least five reductions over the potential window investigated, whereas $[Ru(bpy)_3]^{2+}$ undergoes only three. For **Ru-1T**−**Ru-4T**, the additional oxidation due to the thienyl group ($nT^{0/+}$) occurs before Ru^2 oxidation. **Ru-2T**−**Ru-4T** underwent additional reductions involving their *n*T groups: one for **Ru-2T**, two for **Ru-3T**, and three for **Ru-4T**. The most redox-active of the series, **Ru-4T**, undergoes two oxidations and eight reductions over the potential window investigated.

Only complexes with thiophenes are phototoxic toward melanoma cells (SK-MEL-28), with potency increasing with n. **Ru-4T** demonstrated EC_{50} values in the low-nanomolar regime and PIs around 10^4 in normoxia under visible light. Notably, all values fell within an order of magnitude of each other over six biological replicates. Both **Ru-3T** and **Ru-4T** retain some of this activity in hypoxia, where **Ru-4T** has a visible EC_{50} as low as 35 nM and PI as high as 2900. These results highlight the significance of lowest-lying ^{3}ILCT states for enhancing phototoxicity toward cancer cells and maintaining activity in hypoxia. This family illustrates that Ru(II) coordinated to IP-3T or IP-4T ligands results in an excellent pharmacophore that can tolerate a variety of changes to the polypyridyl ancillary ligands. In this case, the redox activity of the system is changed substantially by the 4,4′-btfmb coligands (compared to our previously published analogues), and the complexes with three or four thiophene rings were still of high potency. The fluorinated polypyridyl ligands are of ongoing interest given the important role that fluorinated groups play in medicinal chemistry. These findings highlight **Ru-4T** as an excellent candidate for further investigations.

■ ASSOCIATED CONTENT

Supporting Information

The Supporting Information is available free of charge at https://pubs.acs.org/doi/10.1021/acs.inorgchem.3c04382.

Synthetic characterization (1D and 2D NMR, HPLC, and HRMS); computational details and additional results; spectroscopic characterization (emission and TA); electrochemical characterization; and (photo)-biological data (PDF)

■ AUTHOR INFORMATION

Corresponding Authors

Marta E. Alberto − *Dipartimento di Chimica e Tecnologie Chimiche, Università della Calabria, Arcavacata di Rende 87036, Italy;* orcid.org/0000-0001-9925-7233; Email: marta.alberto@unical.it

Colin G. Cameron − *Department of Chemistry and Biochemistry, The University of Texas at Arlington, Arlington, Texas 76019-0065, United States;* orcid.org/0000-0003-0978-0894; Email: colin.cameron@uta.edu

Sherri A. McFarland − *Department of Chemistry and Biochemistry, The University of Texas at Arlington, Arlington, Texas 76019-0065, United States;* orcid.org/0000-0002-8028-5055; Email: sherri.mcfarland@uta.edu

Authors

Houston D. Cole − *Department of Chemistry and Biochemistry, The University of Texas at Arlington, Arlington, Texas 76019-0065, United States;* orcid.org/0000-0002-2922-2163

Abbas Vali − *Department of Chemistry and Biochemistry, The University of Texas at Arlington, Arlington, Texas 76019-0065, United States*

John A. Roque, III − *Department of Chemistry and Biochemistry, The University of Texas at Arlington, Arlington, Texas 76019-0065, United States*

Ge Shi − *Department of Chemistry and Biochemistry, The University of Texas at Arlington, Arlington, Texas 76019-0065, United States*

Alisher Talgatov − *Department of Chemistry and Biochemistry, The University of Texas at Arlington, Arlington, Texas 76019-0065, United States*

https://doi.org/10.1021/acs.inorgchem.3c04382
Inorg. Chem. XXXX, XXX, XXX−XXX

Gurleen Kaur − *Department of Chemistry and Biochemistry, The University of Texas at Arlington, Arlington, Texas 76019-0065, United States;* orcid.org/0009-0009-0532-8041

Antonio Francés-Monerris − *Institut de Ciència Molecular, Universitat de València, 46071 València, Spain;* orcid.org/0000-0001-8232-4989

Complete contact information is available at: https://pubs.acs.org/10.1021/acs.inorgchem.3c04382

Notes

The authors declare the following competing financial interest(s): S.A.M. has a potential research conflict of interest due to a financial interest with Theralase Technologies, Inc. and PhotoDynamic, Inc. A management plan has been created to preserve objectivity in research in accordance with UTA policy.

■ ACKNOWLEDGMENTS

S.A.M. and C.G.C. thank the National Cancer Institute (NCI) of the National Institutes of Health (NIH) (Award R01CA222227) and the National Science Foundation (NSF) (Award NSF 2102459) for support. The content in this work is solely the responsibility of the authors and does not necessarily represent the official views of the National Institutes of Health. S.A.M. also thanks Dr. Daniel Todd as UNCG's Triad Mass Spectrometry Facility manager and his assistants Jennifer Simpson and Diane Wallace. S.A.M. likewise thanks Dr. Franklin Moy (UNCG) and Dr. Brian Edwards (UTA) for their experimental support and instrument maintenance as NMR facility managers. A.F.-M. thanks the Grant PID2021-127554NA-I00 funded by the Spanish Ministry of Science and Innovation (MCIN/AEI/10.13039/501100011033) and by "ERDF A way of making Europe." M.E.A. acknowledges the CINECA award under the ISCRA initiative (HyPS4DAT Project) for the availability of high-performance computing resources.

■ REFERENCES

(1) Sung, H.; Ferlay, J.; Siegel, R. L.; Laversanne, M.; Soerjomataram, I.; Jemal, A.; Bray, F. Global Cancer Statistics 2020: GLOBOCAN Estimates of Incidence and Mortality Worldwide for 36 Cancers in 185 Countries. *Ca-Cancer J. Clin.* **2021**, *71* (3), 209−249.

(2) Mellman, I.; Coukos, G.; Dranoff, G. Cancer Immunotherapy Comes of Age. *Nature* **2011**, *480* (7378), 480−489.

(3) Marabelle, A.; Tselikas, L.; De Baere, T.; Houot, R. Intratumoral Immunotherapy: Using the Tumor as the Remedy. *Ann. Oncol.* **2017**, *28*, xii33−xii43.

(4) Meric-Bernstam, F.; Larkin, J.; Tabernero, J.; Bonini, C. Enhancing Anti-Tumour Efficacy with Immunotherapy Combinations. *Lancet* **2021**, *397* (10278), 1010−1022.

(5) Sawyers, C. Targeted Cancer Therapy. *Nature* **2004**, *432* (7015), 294−297.

(6) Min, H.-Y.; Lee, H.-Y. Molecular Targeted Therapy for Anticancer Treatment. *Exp. Mol. Med.* **2022**, *54* (10), 1670−1694.

(7) Mroz, P.; Hashmi, J. T.; Huang, Y.-Y.; Lange, N.; Hamblin, M. R. Stimulation of Anti-Tumor Immunity by Photodynamic Therapy. *Expert Rev. Clin. Immunol.* **2011**, *7* (1), 75−91.

(8) Anzengruber, F.; Avci, P.; de Freitas, L. F.; Hamblin, M. R. T-Cell Mediated Anti-Tumor Immunity after Photodynamic Therapy: Why Does It Not Always Work and How Can We Improve It. *Photochem. Photobiol. Sci.* **2015**, *14* (8), 1492−1509.

(9) Gollnick, S. O.; Brackett, C. M. Enhancement of Anti-Tumor Immunity by Photodynamic Therapy. *Immunol. Res.* **2010**, *46* (1−3), 216−226.

(10) Gollnick, S. O. Photodynamic Therapy and Antitumor Immunity. *J. Natl. Compr. Cancer Network* **2012**, *10* (Suppl 2), S40−S43.

(11) Monro, S.; Colón, K. L.; Yin, H.; Roque, J.; Konda, P.; Gujar, S.; Thummel, R. P.; Lilge, L.; Cameron, C. G.; McFarland, S. A. Transition Metal Complexes and Photodynamic Therapy from a Tumor-Centered Approach: Challenges, Opportunities, and Highlights from the Development of TLD1433. *Chem. Rev.* **2019**, *119* (2), 797−828.

(12) McFarland, S. A.; Mandel, A.; Dumoulin-White, R.; Gasser, G. Metal-Based Photosensitizers for Photodynamic Therapy: The Future of Multimodal Oncology? *Curr. Opin. Chem. Biol.* **2020**, *56*, 23−27.

(13) Howerton, B. S.; Heidary, D. K.; Glazer, E. C. Strained Ruthenium Complexes Are Potent Light-Activated Anticancer Agents. *J. Am. Chem. Soc.* **2012**, *134* (20), 8324−8327.

(14) Sainuddin, T.; Pinto, M.; Yin, H.; Hetu, M.; Colpitts, J.; McFarland, S. A. Strained Ruthenium Metal−Organic Dyads as Photocisplatin Agents with Dual Action. *J. Inorg. Biochem.* **2016**, *158*, 45−54.

(15) Roque, J.; Havrylyuk, D.; Barrett, P. C.; Sainuddin, T.; McCain, J.; Colón, K.; Sparks, W. T.; Bradner, E.; Monro, S.; Heidary, D.; Cameron, C. G.; Glazer, E. C.; McFarland, S. A. Strained, Photoejecting Ru(II) Complexes That Are Cytotoxic Under Hypoxic Conditions. *Photochem. Photobiol.* **2020**, *96* (2), 327−339.

(16) Cole, H. D.; Roque, J. A.; Lifshits, L. M.; Hodges, R.; Barrett, P. C.; Havrylyuk, D.; Heidary, D.; Ramasamy, E.; Cameron, C. G.; Glazer, E. C.; McFarland, S. A. Fine-Feature Modifications to Strained Ruthenium Complexes Radically Alter Their Hypoxic Anticancer Activity. *Photochem. Photobiol.* **2022**, *98* (1), 73−84.

(17) Roque, J. A., III; Cole, H. D.; Barrett, P. C.; Lifshits, L. M.; Hodges, R. O.; Kim, S.; Deep, G.; Francés-Monerris, A.; Alberto, M. E.; Cameron, C. G.; McFarland, S. A. Intraligand Excited States Turn a Ruthenium Oligothiophene Complex into a Light-Triggered Ubertoxin with Anticancer Effects in Extreme Hypoxia. *J. Am. Chem. Soc.* **2022**, *144* (18), 8317−8336.

(18) Cuello-Garibo, J.-A.; Meijer, M. S.; Bonnet, S. To Cage or to Be Caged? The Cytotoxic Species in Ruthenium-Based Photoactivated Chemotherapy Is Not Always the Metal. *Chem. Commun.* **2017**, *53* (50), 6768−6771.

(19) Azar, D. F.; Audi, H.; Farhat, S.; El-Sibai, M.; Abi-Habib, R. J.; Khnayzer, R. S. Phototoxicity of Strained Ru(II) Complexes: Is It the Metal Complex or the Dissociating Ligand? *Dalton Trans.* **2017**, *46* (35), 11529−11532.

(20) Cole, H. D.; Roque, J. A.; Shi, G.; Lifshits, L. M.; Ramasamy, E.; Barrett, P. C.; Hodges, R. O.; Cameron, C. G.; McFarland, S. A. Anticancer Agent with Inexplicable Potency in Extreme Hypoxia: Characterizing a Light-Triggered Ruthenium Ubertoxin. *J. Am. Chem. Soc.* **2022**, *144* (22), 9543−9547.

(21) Sun, Y.; Heidary, D. K.; Zhang, Z.; Richards, C. I.; Glazer, E. C. Bacterial Cytological Profiling Reveals the Mechanism of Action of Anticancer Metal Complexes. *Mol. Pharmaceutics* **2018**, *15* (8), 3404−3416.

(22) Loftus, L. M.; White, J. K.; Albani, B. A.; Kohler, L.; Kodanko, J. J.; Thummel, R. P.; Dunbar, K. R.; Turro, C. New Ru^{II} Complex for Dual Activity: Photoinduced Ligand Release and $^1O_2$ Production. *Chem.—Eur. J.* **2016**, *22* (11), 3704−3708.

(23) Toupin, N. P.; Nadella, S.; Steinke, S. J.; Turro, C.; Kodanko, J. J. Dual-Action Ru(II) Complexes with Bulky π-Expansive Ligands: Phototoxicity without DNA Intercalation. *Inorg. Chem.* **2020**, *59* (6), 3919−3933.

(24) Lameijer, L. N.; Ernst, D.; Hopkins, S. L.; Meijer, M. S.; Askes, S. H. C.; Le Dévédec, S. E.; Bonnet, S. A Red-Light-Activated Ruthenium-Caged NAMPT Inhibitor Remains Phototoxic in Hypoxic Cancer Cells. *Angew. Chem., Int. Ed.* **2017**, *56* (38), 11549−11553.

(25) Albani, B. A.; Durr, C. B.; Turro, C. Selective Photoinduced Ligand Exchange in a New Tris−Heteroleptic Ru(II) Complex. *J. Phys. Chem. A* **2013**, *117* (50), 13885−13892.
(26) Knoll, J. D.; Albani, B. A.; Durr, C. B.; Turro, C. Unusually Efficient Pyridine Photodissociation from Ru(II) Complexes with Sterically Bulky Bidentate Ancillary Ligands. *J. Phys. Chem. A* **2014**, *118* (45), 10603−10610.
(27) Arora, K.; White, J. K.; Sharma, R.; Mazumder, S.; Martin, P. D.; Schlegel, H. B.; Turro, C.; Kodanko, J. J. Effects of Methyl Substitution in Ruthenium Tris(2-Pyridylmethyl)Amine Photocaging Groups for Nitriles. *Inorg. Chem.* **2016**, *55* (14), 6968−6979.
(28) Huisman, M.; White, J. K.; Lewalski, V. G.; Podgorski, I.; Turro, C.; Kodanko, J. J. Caging the Uncageable: Using Metal Complex Release for Photochemical Control over Irreversible Inhibition. *Chem. Commun.* **2016**, *52* (85), 12590−12593.
(29) Li, A.; Yadav, R.; White, J. K.; Herroon, M. K.; Callahan, B. P.; Podgorski, I.; Turro, C.; Scott, E. E.; Kodanko, J. J. Illuminating Cytochrome P450 Binding: Ru(II)-Caged Inhibitors of CYP17A1. *Chem. Commun.* **2017**, *53* (26), 3673−3676.
(30) Arora, K.; Herroon, M.; Al-Afyouni, M. H.; Toupin, N. P.; Rohrabaugh, T. N.; Loftus, L. M.; Podgorski, I.; Turro, C.; Kodanko, J. J. Catch and Release Photosensitizers: Combining Dual-Action Ruthenium Complexes with Protease Inactivation for Targeting Invasive Cancers. *J. Am. Chem. Soc.* **2018**, *140* (43), 14367−14380.
(31) Li, A.; Turro, C.; Kodanko, J. J. Ru(II) Polypyridyl Complexes Derived from Tetradentate Ancillary Ligands for Effective Photocaging. *Acc. Chem. Res.* **2018**, *51* (6), 1415−1421.
(32) Li, A.; Turro, C.; Kodanko, J. J. Ru(II) Polypyridyl Complexes as Photocages for Bioactive Compounds Containing Nitriles and Aromatic Heterocycles. *Chem. Commun.* **2018**, *54* (11), 1280−1290.
(33) Nisbett, K.; Tu, Y.-J.; Turro, C.; Kodanko, J. J.; Schlegel, H. B. DFT Investigation of Ligand Photodissociation in $[Ru^{II}(tpy)(bpy)(py)]^{2+}$ and $[Ru^{II}(tpy)(Me_2bpy)(py)]^{2+}$ Complexes. *Inorg. Chem.* **2018**, *57* (1), 231−240.
(34) Rohrabaugh, T. N.; Rohrabaugh, A. M.; Kodanko, J. J.; White, J. K.; Turro, C. Photoactivation of Imatinib−Antibody Conjugate Using Low-Energy Visible Light from Ru(II)-Polypyridyl Cages. *Chem. Commun.* **2018**, *54* (41), 5193−5196.
(35) Bahreman, A.; Limburg, B.; Siegler, M. A.; Bouwman, E.; Bonnet, S. Spontaneous Formation in the Dark, and Visible Light-Induced Cleavage, of a Ru−S Bond in Water: A Thermodynamic and Kinetic Study. *Inorg. Chem.* **2013**, *52* (16), 9456−9469.
(36) Bahreman, A.; Rabe, M.; Kros, A.; Bruylants, G.; Bonnet, S. Binding of a Ruthenium Complex to a Thioether Ligand Embedded in a Negatively Charged Lipid Bilayer: A Two-Step Mechanism. *Chem.—Eur. J.* **2014**, *20* (24), 7429−7438.
(37) Göttle, A. J.; Alary, F.; Boggio-Pasqua, M.; Dixon, I. M.; Heully, J.-L.; Bahreman, A.; Askes, S. H. C.; Bonnet, S. Pivotal Role of a Pentacoordinate ^{3}MC State on the Photocleavage Efficiency of a Thioether Ligand in Ruthenium(II) Complexes: A Theoretical Mechanistic Study. *Inorg. Chem.* **2016**, *55* (9), 4448−4456.
(38) Cuello-Garibo, J.-A.; Pérez-Gallent, E.; van der Boon, L.; Siegler, M. A.; Bonnet, S. Influence of the Steric Bulk and Solvent on the Photoreactivity of Ruthenium Polypyridyl Complexes Coordinated to L-Proline. *Inorg. Chem.* **2017**, *56* (9), 4818−4828.
(39) Sun, W.; Wen, Y.; Thiramanas, R.; Chen, M.; Han, J.; Gong, N.; Wagner, M.; Jiang, S.; Meijer, M. S.; Bonnet, S.; Butt, H.-J.; Mailänder, V.; Liang, X.-J.; Wu, S. Red-Light-Controlled Release of Drug-Ru Complex Conjugates from Metallopolymer Micelles for Phototherapy in Hypoxic Tumor Environments. *Adv. Funct. Mater.* **2018**, *28* (39), No. 1804227.
(40) Meijer, M. S.; Talens, V. S.; Hilbers, M. F.; Kieltyka, R. E.; Brouwer, A. M.; Natile, M. M.; Bonnet, S. NIR-Light-Driven Generation of Reactive Oxygen Species Using Ru(II)-Decorated Lipid-Encapsulated Upconverting Nanoparticles. *Langmuir* **2019**, *35* (37), 12079−12090.
(41) Havrylyuk, D.; Hachey, A. C.; Fenton, A.; Heidary, D. K.; Glazer, E. C. Ru(II) Photocages Enable Precise Control over Enzyme Activity with Red Light. *Nat. Commun.* **2022**, *13* (1), No. 3636.
(42) Ryan, R. T.; Havrylyuk, D.; Stevens, K. C.; Moore, L. H.; Parkin, S.; Blackburn, J. S.; Heidary, D. K.; Selegue, J. P.; Glazer, E. C. Biological Investigations of Ru(II) Complexes with Diverse β-Diketone Ligands. *Eur. J. Inorg. Chem.* **2021**, *2021* (35), 3611−3621.
(43) Wachter, E.; Heidary, D. K.; Howerton, B. S.; Parkin, S.; Glazer, E. C. Light-Activated Ruthenium Complexes Photobind DNA and Are Cytotoxic in the Photodynamic Therapy Window. *Chem. Commun.* **2012**, *48* (77), 9649.
(44) Huang, H.; Banerjee, S.; Qiu, K.; Zhang, P.; Blacque, O.; Malcomson, T.; Paterson, M. J.; Clarkson, G. J.; Staniforth, M.; Stavros, V. G.; Gasser, G.; Chao, H.; Sadler, P. J. Targeted Photoredox Catalysis in Cancer Cells. *Nat. Chem.* **2019**, *11* (11), 1041−1048.
(45) Baptista, M. S.; Cadet, J.; Di Mascio, P.; Ghogare, A. A.; Greer, A.; Hamblin, M. R.; Lorente, C.; Nunez, S. C.; Ribeiro, M. S.; Thomas, A. H.; Vignoni, M.; Yoshimura, T. M. Type I and Type II Photosensitized Oxidation Reactions: Guidelines and Mechanistic Pathways. *Photochem. Photobiol.* **2017**, *93* (4), 912−919.
(46) Roque, J. A., III; Barrett, P. C.; Cole, H. D.; Lifshits, L. M.; Shi, G.; Monro, S.; von Dohlen, D.; Kim, S.; Russo, N.; Deep, G.; Cameron, C. G.; Alberto, M. E.; McFarland, S. A. Breaking the Barrier: An Osmium Photosensitizer with Unprecedented Hypoxic Phototoxicity for Real World Photodynamic Therapy. *Chem. Sci.* **2020**, *11*, 9784−9806.
(47) Shi, G.; Monro, S.; Hennigar, R.; Colpitts, J.; Fong, J.; Kasimova, K.; Yin, H.; DeCoste, R.; Spencer, C.; Chamberlain, L.; Mandel, A.; Lilge, L.; McFarland, S. A. Ru(II) Dyads Derived from α-Oligothiophenes: A New Class of Potent and Versatile Photosensitizers for PDT. *Coord. Chem. Rev.* **2015**, *282*−*283*, 127−138.
(48) Kulkarni, G. S.; Lilge, L.; Nesbitt, M.; Dumoulin-White, R. J.; Mandel, A.; Jewett, M. A. S. A Phase 1b Clinical Study of Intravesical Photodynamic Therapy in Patients with Bacillus Calmette-Guérin−Unresponsive Non−Muscle-Invasive Bladder Cancer. *Eur. Urol. Open Sci.* **2022**, *41*, 105−111.
(49) Roque, J. A.; Barrett, P. C.; Cole, H. D.; Lifshits, L. M.; Bradner, E.; Shi, G.; von Dohlen, D.; Kim, S.; Russo, N.; Deep, G.; Cameron, C. G.; Alberto, M. E.; McFarland, S. A. Os(II) Oligothienyl Complexes as a Hypoxia-Active Photosensitizer Class for Photodynamic Therapy. *Inorg. Chem.* **2020**, *59* (22), 16341−16360.
(50) Lifshits, L. M.; Roque, J. A.; Cole, H. D.; Thummel, R. P.; Cameron, C. G.; McFarland, S. A. NIR-Absorbing Ru II Complexes Containing α-Oligothiophenes for Applications in Photodynamic Therapy. *ChemBioChem* **2020**, *21*, 3594−3607.
(51) Cole, H. D.; Vali, A.; Roque, J. A.; Shi, G.; Kaur, G.; Hodges, R. O.; Francés-Monerris, A.; Alberto, M. E.; Cameron, C. G.; McFarland, S. A. Ru(II) Phenanthroline-Based Oligothienyl Complexes as Phototherapy Agents. *Inorg. Chem.* **2023**, *62* (51), 21181−21200.
(52) Armstrong, D. W.; Yu, J.; Cole, H. D.; McFarland, S. A.; Nafie, J. Chiral Resolution and Absolute Configuration Determination of New Metal-Based Photodynamic Therapy Antitumor Agents. *J. Pharm. Biomed. Anal.* **2021**, *204*, No. 114233.
(53) Handlovic, T. T.; Wahab, M. F.; Cole, H. D.; Alatrash, N.; Ramasamy, E.; MacDonnell, F. M.; McFarland, S. A.; Armstrong, D. W. Insights into Enantioselective Separations of Ionic Metal Complexes by Sub/Supercritical Fluid Chromatography. *Anal. Chim. Acta* **2022**, *1228*, No. 340156.
(54) Farney, E. P.; Chapman, S. J.; Swords, W. B.; Torelli, M. D.; Hamers, R. J.; Yoon, T. P. Discovery and Elucidation of Counteranion Dependence in Photoredox Catalysis. *J. Am. Chem. Soc.* **2019**, *141* (15), 6385−6391.
(55) Furue, M.; Maruyama, K.; Oguni, T.; Naiki, M.; Kamachi, M. Trifluoromethyl-Substituted 2,2′-Bipyridine Ligands. Synthetic Control of Excited-State Properties of Ruthenium(II) Tris-Chelate Complexes. *Inorg. Chem.* **1992**, *31* (18), 3792−3795.
(56) Maurer, A. B.; Piechota, E. J.; Meyer, G. J. Excited-State Dipole Moments of Homoleptic $[Ru(Bpy')_3]^{2+}$ Complexes Measured by Stark Spectroscopy. *J. Phys. Chem. A* **2019**, *123* (41), 8745−8754.

https://doi.org/10.1021/acs.inorgchem.3c04382
Inorg. Chem. XXXX, XXX, XXX−XXX

(57) Nomrowski, J.; Wenger, O. S. Photoinduced PCET in Ruthenium−Phenol Systems: Thermodynamic Equivalence of Uni- and Bidirectional Reactions. *Inorg. Chem.* **2015**, *54* (7), 3680−3687.
(58) Sullivan, B.; Salmon, D.; Meyer, T. Mixed Phosphine 2,2′-Bipyridine Complexes of Ruthenium. *Inorg. Chem.* **1978**, *17* (12), 3334−3341.
(59) Wang, Z. *Comprehensive Organic Name Reactions and Reagents*; John Wiley & Sons, Inc.: Hoboken, NJ, USA, 2010. DOI: 10.1002/9780470638859.
(60) Ghosh, G.; Colón, K. L.; Fuller, A.; Sainuddin, T.; Bradner, E.; McCain, J.; Monro, S. M. A.; Yin, H.; Hetu, M. W.; Cameron, C. G.; McFarland, S. A. Cyclometalated Ruthenium(II) Complexes Derived from α-Oligothiophenes as Highly Selective Cytotoxic or Photocytotoxic Agents. *Inorg. Chem.* **2018**, *57* (13), 7694−7712.
(61) Chen, R.; Yang, X.; Tian, H.; Wang, X.; Hagfeldt, A.; Sun, L. Effect of Tetrahydroquinoline Dyes Structure on the Performance of Organic Dye-Sensitized Solar Cells. *Chem. Mater.* **2007**, *19* (16), 4007−4015.
(62) Casida, M. E. Time−Dependent Density Functional Response Theory of Molecular Systems: Theory, Computational Methods, and Functionals. In *Recent Developments and Applications of Modern Density Functional Theory*; Seminario, J. M., Ed.; Theoretical and computational chemistry; Elsevier: Amsterdam; Netherlands, 1996; pp 155−192.
(63) Frisch, M. J.; Trucks, G. W.; Schlegel, H. B.; Scuseria, G. E.; Robb, M. A.; Cheeseman, J. R.; Scalmani, G.; Barone, V.; Petersson, G. A.; Nakatsuji, H.; Li, X.; Caricato, M.; Marenich, A. V.; Bloino, J.; Janesko, B. G.; Gomperts, R.; Mennucci, B.; Hratchian, H. P.; Ortiz, J. V.; Izmaylov, A. F.; Sonnenberg, J. L.; Williams-Young, D.; Ding, F.; Lipparini, F.; Egidi, F.; Goings, J.; Peng, B.; Petrone, A.; Henderson, T.; Ranasinghe, D.; Zakrzewski, V. G.; Gao, J.; Rega, N.; Zheng, G.; Liang, W.; Hada, M.; Ehara, M.; Toyota, K.; Fukuda, R.; Hasegawa, J.; Ishida, M.; Nakajima, T.; Honda, Y.; Kitao, O.; Nakai, H.; Vreven, T.; Throssell, K.; Montgomery, J. A., Jr.; Peralta, J. E.; Ogliaro, F.; Bearpark, M. J.; Heyd, J. J.; Brothers, E. N.; Kudin, K. N.; Staroverov, V. N.; Keith, T. A.; Kobayashi, R.; Normand, J.; Raghavachari, K.; Rendell, A. P.; Burant, J. C.; Iyengar, S. S.; Tomasi, J.; Cossi, M.; Millam, J. M.; Klene, M.; Adamo, C.; Cammi, R.; Ochterski, J. W.; Martin, R. L.; Morokuma, K.; Farkas, O.; Foresman, J. B.; Fox, D. J. *Gaussian 16, Revision C.01*, 2016.
(64) Ponte, F.; Alberto, M. E.; De Simone, B. C.; Russo, N.; Sicilia, E. Photophysical Exploration of Dual-Approach Pt^{II}−BODIPY Conjugates: Theoretical Insights. *Inorg. Chem.* **2019**, *58* (15), 9882−9889.
(65) Alberto, M. E.; Francés-Monerris, A. A Multiscale Free Energy Method Reveals an Unprecedented Photoactivation of a Bimetallic Os(ii)−Pt(ii) Dual Anticancer Agent. *Phys. Chem. Chem. Phys.* **2022**, *24* (32), 19584−19594.
(66) Alberto, M. E.; Russo, N.; Adamo, C. Synergistic Effects of Metals in a Promising Ru^{II}−Pt^{II} Assembly for a Combined Anticancer Approach: Theoretical Exploration of the Photophysical Properties. *Chem.—Eur. J.* **2016**, *22* (27), 9162−9168.
(67) Alberto, M. E.; Pirillo, J.; Russo, N.; Adamo, C. Theoretical Exploration of Type I/Type II Dual Photoreactivity of Promising Ru(II) Dyads for PDT Approach. *Inorg. Chem.* **2016**, *55* (21), 11185−11192.
(68) Bertini, L.; Alberto, M. E.; Arrigoni, F.; Vertemara, J.; Fantucci, P.; Bruschi, M.; Zampella, G.; De Gioia, L. On the Photochemistry of $Fe_2(Edt)(CO)_4(PMe_3)_2$, a [FeFe]-Hydrogenase Model: A DFT/TDDFT Investigation. *Int. J. Quantum Chem.* **2018**, *118* (9), No. e25537.
(69) Alberto, M. E.; Adamo, C. Synergistic Effects in Pt^{II}-Porphyrinoid Dyes as Candidates for a Dual-Action Anticancer Therapy: A Theoretical Exploration. *Chem.—Eur. J.* **2017**, *23* (60), 15124−15132.
(70) Francés-Monerris, A.; Magra, K.; Darari, M.; Cebrián, C.; Beley, M.; Domenichini, E.; Haacke, S.; Pastore, M.; Assfeld, X.; Gros, P. C.; Monari, A. Synthesis and Computational Study of a Pyridylcarbene Fe(II) Complex: Unexpected Effects of *Fac*/*Mer* Isomerism in Metal-to-Ligand Triplet Potential Energy Surfaces. *Inorg. Chem.* **2018**, *57* (16), 10431−10441.
(71) Alberto, M. E.; Mazzone, G.; Regina, C.; Russo, N.; Sicilia, E. Theoretical Exploration of the Photophysical Properties of Two-Component Ru^{II}−Porphyrin Dyes as Promising Assemblies for a Combined Antitumor Effect. *Dalton Trans.* **2020**, *49* (36), 12653−12661.
(72) Adamo, C.; Barone, V. Toward Reliable Density Functional Methods without Adjustable Parameters: The PBE0Model. *J. Chem. Phys.* **1999**, *110* (13), 6158−6170.
(73) Andrae, D.; Häußermann, U.; Dolg, M.; Stoll, H.; Preuß, H. Energy-Adjusted Ab Initio Pseudopotentials for the Second and Third Row Transition Elements. *Theor. Chim. Acta* **1990**, *77* (2), 123−141.
(74) Hirata, S.; Head-Gordon, M. Time-Dependent Density Functional Theory within the Tamm−Dancoff Approximation. *Chem. Phys. Lett.* **1999**, *314* (3−4), 291−299.
(75) Peach, M. J. G.; Williamson, M. J.; Tozer, D. J. Influence of Triplet Instabilities in TDDFT. *J. Chem. Theory Comput.* **2011**, *7* (11), 3578−3585.
(76) Cossi, M.; Barone, V. Solvent Effect on Vertical Electronic Transitions by the Polarizable Continuum Model. *J. Chem. Phys.* **2000**, *112* (5), 2427−2435.
(77) Tomasi, J.; Mennucci, B.; Cammi, R. Quantum Mechanical Continuum Solvation Models. *Chem. Rev.* **2005**, *105* (8), 2999−3094.
(78) Cossi, M.; Rega, N.; Scalmani, G.; Barone, V. Energies, Structures, and Electronic Properties of Molecules in Solution with the C-PCM Solvation Model. *J. Comput. Chem.* **2003**, *24* (6), 669−681.
(79) Skripnikov, L. Chemissan. http://www.chemissian.com.
(80) Plasser, F. TheoDORE: A Toolbox for a Detailed and Automated Analysis of Electronic Excited State Computations. *J. Chem. Phys.* **2020**, *152* (8), No. 084108.
(81) Juris, A.; Campagna, S.; Balzani, V.; Gremaud, G.; Von Zelewsky, A. Absorption Spectra, Luminescence Properties, and Electrochemical Behavior of Tris-Heteroleptic Ruthenium(II) Polypyridine Complexes. *Inorg. Chem.* **1988**, *27* (20), 3652−3655.
(82) Becker, R. S.; Seixas de Melo, J.; Maçanita, A. L.; Elisei, F. Comprehensive Evaluation of the Absorption, Photophysical, Energy Transfer, Structural, and Theoretical Properties of α-Oligothiophenes with One to Seven Rings. *J. Phys. Chem. A* **1996**, *100*, 18683−18695.
(83) DeRosa, M. Photosensitized Singlet Oxygen and Its Applications. *Coord. Chem. Rev.* **2002**, *233*−*234*, 351−371.
(84) Hissler, M.; Connick, W. B.; Geiger, D. K.; McGarrah, J. E.; Lipa, D.; Lachicotte, R. J.; Eisenberg, R. Platinum Diimine Bis(Acetylide) Complexes: Synthesis, Characterization, and Luminescence Properties. *Inorg. Chem.* **2000**, *39* (3), 447−457.
(85) Lincoln, R.; Kohler, L.; Monro, S.; Yin, H.; Stephenson, M.; Zong, R.; Chouai, A.; Dorsey, C.; Hennigar, R.; Thummel, R. P.; McFarland, S. A. Exploitation of Long-Lived ^{3}IL Excited States for Metal−Organic Photodynamic Therapy: Verification in a Metastatic Melanoma Model. *J. Am. Chem. Soc.* **2013**, *135* (45), 17161−17175.
(86) Goze, C.; Kozlov, D. V.; Tyson, D. S.; Ziessel, R.; Castellano, F. N. Synthesis and Photophysics of Ruthenium(Ii) Complexes with Multiple Pyrenylethynylene Subunits. *New J. Chem.* **2003**, *27* (12), 1679.
(87) Monro, S.; Cameron, C. G.; Zhu, X.; Colón, K. L.; Yin, H.; Sainuddin, T.; Hetu, M.; Pinto, M.; Fuller, A.; Bennett, L.; Roque, J.; Sun, W.; McFarland, S. A. Synthesis, Characterization and Photobiological Studies of Ru(II) Dyads Derived from α-Oligothiophene Derivatives of 1,10-Phenanthroline. *Photochem. Photobiol.* **2019**, *95* (1), 267−279.
(88) Chettri, A.; Schneider, K. R. A.; Cole, H. D.; Roque, J. A.; Cameron, C. G.; McFarland, S. A.; Dietzek, B. String-Attached Oligothiophene Substituents Determine the Fate of Excited States in Ruthenium Complexes for Photodynamic Therapy. *J. Phys. Chem. A* **2021**, *125* (32), 6985−6994.
(89) Chettri, A.; Roque, J. A.; Schneider, K. R. A.; Cole, H. D.; Cameron, C. G.; McFarland, S. A.; Dietzek, B. It Takes Three to Tango: The Length of the Oligothiophene Chain Determines the

https://doi.org/10.1021/acs.inorgchem.3c04382
Inorg. Chem. XXXX, XXX, XXX−XXX

Nature of the Long-Lived Excited State and the Resulting Photocytotoxicity of a Ruthenium(II) Photodrug. *ChemPhotoChem* **2021**, *5* (5), 421−425.
(90) McClenaghan, N. D.; Leydet, Y.; Maubert, B.; Indelli, M. T.; Campagna, S. Excited-State Equilibration: A Process Leading to Long-Lived Metal-to-Ligand Charge Transfer Luminescence in Supramolecular Systems. *Coord. Chem. Rev.* **2005**, *249* (13−14), 1336−1350.
(91) Juris, A.; Balzani, V.; Barigelletti, F.; Campagna, S.; Belser, P.; von Zelewsky, A. Ru(II) Polypyridine Complexes: Photophysics, Photochemistry, Eletrochemistry, and Chemiluminescence. *Coord. Chem. Rev.* **1988**, *84*, 85−277.
(92) Ohsawa, Y.; DeArmond, M. K.; Hanck, K. W.; Morris, D. E.; Whitten, D. G.; Neveux, P. E. Spatially Isolated Redox Orbitals: Evidence from Low-Temperature Voltammetry. *J. Am. Chem. Soc.* **1983**, *105* (21), 6522−6524.
(93) Ohsawa, Y.; Hanck, K. W.; DeArmond, M. K. A Systematic Electrochemical and Spectroscopic Study of Mixed-Ligand Ruthenium(II) 2,2′-Bipyridine Complexes $[Ru(bpy)_{3-n}L_n]^{2+}$ (n = 0, 1, 2 and 3). *J. Electroanal. Chem. Interfacial Electrochem.* **1984**, *175* (1−2), 229−240.
(94) Roncali, J. Conjugated Poly(Thiophenes): Synthesis, Functionalization, and Applications. *Chem. Rev.* **1992**, *92* (4), 711−738.
(95) Pavlishchuk, V. V.; Addison, A. W. Conversion Constants for Redox Potentials Measured versus Different Reference Electrodes in Acetonitrile Solutions at 25°C. *Inorg. Chim. Acta* **2000**, *298* (1), 97−102.
(96) Diaz, A. F.; Crowley, J.; Bargon, J.; Gardini, G. P.; Torrance, J. B. Electrooxidation of Aromatic Oligomers and Conducting Polymers. *J. Electroanal. Chem. Interfacial Electrochem.* **1981**, *121*, 355−361.
(97) Yin, H.; Stephenson, M.; Gibson, J.; Sampson, E.; Shi, G.; Sainuddin, T.; Monro, S.; McFarland, S. A. In Vitro Multiwavelength PDT with ^{3}IL States: Teaching Old Molecules New Tricks. *Inorg. Chem.* **2014**, *53* (9), 4548−4559.

https://doi.org/10.1021/acs.inorgchem.3c04382
Inorg. Chem. XXXX, XXX, XXX−XXX